The Astrophysical Journal, 797:90 (28pp), 2014 December 20 doi:10.1088/0004-637X/797/2/90

AN INFRARED-LUMINOUS MERGER WITH TWO BIPOLAR MOLECULAR OUTFLOWS: ALMA AND SMA OBSERVATIONS OF NGC 3256

Kazushi Sakamoto[1], Susanne Aalto[2], Francoise Combes[3], Aaron Evans[4,5], and Alison Peck[4]
[1] Academia Sinica, Institute of Astronomy and Astrophysics, Taipei, Taiwan
[2] Department of Earth and Space Sciences, Chalmers University of Technology, Onsala Space Observatory, Onsala, Sweden
[3] Observatoire de Paris, 61 Av. de l'Observatoire, F-75014 Paris, France
[4] NRAO, 520 Edgemont Road, Charlottesville, VA 22903, USA
[5] University of Virginia, Charlottesville, VA 22904, USA
Received 2014 March 4; accepted 2014 October 1; published 2014 December 3

ABSTRACT

We report Atacama Large Millimeter/sub-millimeter Array and Submillimeter Array observations of the infrared-luminous merger NGC 3256, the most luminous galaxy within $z = 0.01$. Both of the two merger nuclei separated by $5''$ (0.8 kpc) have a molecular gas concentration, a nuclear disk, with $\Sigma_{\rm mol} > 10^3\,M_\odot\,{\rm pc}^{-2}$. The northern nucleus is more massive and is surrounded by molecular spiral arms. Its nuclear disk is face-on, while the southern nuclear disk is almost edge-on. The high-velocity molecular gas in the system can be resolved into two molecular outflows from the two nuclei. The one from the northern nucleus is part of a starburst-driven superwind seen nearly pole-on. Its maximum velocity is $>750\,{\rm km\,s^{-1}}$ and its mass outflow rate is $>60\,M_\odot\,{\rm yr^{-1}}$ for a conversion factor $X_{\rm CO} = N_{\rm H_2}/I_{\rm CO(1-0)}$ of $1 \times 10^{20}\,{\rm cm^{-2}\,(K\,km\,s^{-1})^{-1}}$. The molecular outflow from the southern nucleus is a highly collimated bipolar jet seen nearly edge-on. Its line-of-sight velocity increases with distance, out to 300 pc from the nucleus, to the maximum de-projected velocity of $\sim 2000\,{\rm km\,s^{-1}}$ for the estimated inclination and $\gtrsim 1000\,{\rm km\,s^{-1}}$ taking into account the uncertainty. Its mass outflow rate is estimated to be $>50\,M_\odot\,{\rm yr^{-1}}$ for the same $X_{\rm CO}$. This southern outflow has indications of being driven by a bipolar radio jet from an active galactic nucleus that recently weakened. The sum of these outflow rates, although subject to the uncertainty in the molecular mass estimate, either exceeds or compares to the total star formation rate. The feedback from nuclear activity through molecular outflows is therefore significant in the gas consumption, and hence evolution, of this system.

Key words: galaxies: active – galaxies: individual (NGC 3256) – galaxies: interactions – galaxies: ISM – ISM: jets and outflows

Online-only material: color figures

1. INTRODUCTION

NGC 3256 is a luminous infrared galaxy with a bolometric luminosity of $L_{\rm bol} = 4 \times 10^{11}\,L_\odot$ ($D = 35$ Mpc, see Table 1 for other parameters). It is a late-stage merger of two disk galaxies and has two nuclei with a projected separation of $5'' = 850$ pc, and two long tidal tails of stars and H I gas (Toomre 1977; Zenner & Lenzen 1993; Norris & Forbes 1995; English et al. 2003). NGC 3256 belongs to the sequence of 'most luminous galaxies within their distance ranges', which are, beyond the local group, NGC 253, M82, NGC 1068, NGC 3256, Arp 299, Arp 220, and Mrk 231 in the catalogue of Sanders et al. (2003) for Galactic latitudes $|b| \geqslant 10^\circ$. It is, therefore, among the best targets to explore luminosity-related phenomena in local galaxies, although its location at decl. $= -44^\circ$ has impeded study.

Sakamoto et al. (2006, hereafter SHP06) made the first interferometric image of CO line emission in NGC 3256 soon after the commissioning of the Submillimeter Array (SMA), and discovered wide CO line wings underlying the much brighter narrow component seen in previous observations (e.g., Sargent et al. 1989; Aalto et al. 2002). The wing emission was attributed to a molecular outflow from the face-on merger. The detection of a galactic molecular outflow from faint and wide CO line wings became possible at that time due in part to the new wide-band capabilities of the SMA. Many extragalactic molecular outflows have been detected since then through broad CO line wings observed with wide-band spectrometers (e.g., Feruglio et al. 2010; Chung et al. 2011; Alatalo et al. 2011).[6] Such molecular outflows coexist with outflows of ionized and atomic gas, and are expected to have significant impact on the luminosity-generation activities in galaxies and the evolution of galaxies themselves (Veilleux et al. 2005; Carilli & Walter 2013, for reviews).

We have used the new Atacama Large Millimeter/sub-millimeter Array (ALMA) in its first open-use semester (Cycle 0) to further study NGC 3256. We aimed at the structure and properties of the molecular gas around the luminous merger nuclei including the high-velocity gas. Although the broad CO wings had been confirmed and found to be even broader in the ALMA commissioning and science verification data (Sakamoto 2013) its structure was still largely unconstrained. We therefore observed the galaxy in the 3 and 0.8 mm bands with ALMA, and also made supplemental 1.3 mm observations with the SMA. We attained much higher angular resolution than previously attained for the circumnuclear molecular gas, up to about $1''$ in CO(1–0), $0\farcs8$ in CO(2–1), and $0\farcs5$ in CO(3–2). We also obtained high quality data of CN(1–0), $\rm CH_3CCH$(6–5), ^{13}CO(2–1),

[6] Detection of molecular outflows from broad OH lines dates back much further (Baan et al. 1989, and references therein). Galactic outflows of cold molecular gas have also been found from off-plane molecular gas of edge-on galaxies (e.g., Nakai et al. 1987 toward M82; Turner 1985, García-Burillo et al. 2000, and Bolatto et al. 2013a toward NGC 253) and from blueshifted molecular absorption lines against nuclear continuum (e.g., Baan et al. 1989; Sakamoto et al. 2009; Fischer et al. 2010, for Arp 220 and Mrk 231). All of these galaxies belong to the previously mentioned unique sequence of luminous nearby galaxies.

Table 1
NGC 3256 Parameters

Parameter	Value	Note
R.A. (J2000)	$10^{h}27^{m}51\overset{s}{.}23$	(1)
Decl. (J2000)	$-43°54'16\overset{''}{.}6$	(1)
V_{sys} (km s^{-1})	2775	(2)
D (Mpc)	35	(3)
Scale. 1″ in pc	170	
$L_{8-1000\,\mu m}$ ($L_\odot$)	$10^{11.56}$	(4)
SFR($M_\odot$ yr^{-1})	50	(5)
p.a. (°)	~70	(6)

Notes. (1) The middle point of the two radio nuclei in Neff et al. (2003). We used this as the center for the ALMA Cycle 0 and SMA observations and for all figures in offset coordinates. The ALMA pointing position for the CSV observations was R.A. = $10^{h}27^{m}51\overset{s}{.}60$, decl. = $-43°54'18\overset{''}{.}0$. (2) Systemic velocity of the merger in radio-definition with respect to the LSR (SHP06). (3) Adopted galaxy distance (Sanders et al. 2003). (4) From the *IRAS* flux data (Sanders et al. 2003). (5) Star formation rate calculated from the bolometric luminosity using the calibration of Murphy et al. (2011) and assuming no AGN contribution. (6) The major-axis position angle of the bulk molecular gas motion in the central ~6 kpc (SHP06).

HCO^{+}(4–3), and the 3 and 0.8 mm continuum. In this paper, we report these new observations and give an overall account of the spatial and kinematic structure of the molecular gas in the center of NGC 3256. We found that the high-velocity gas exists in two bipolar molecular outflows from the two nuclei, and also found that the two outflows are distinctively different from each other. The outflow from the southern nucleus must be a cold-gas counterpart of the outflow of hot molecular gas from the same nucleus discovered by Emonts et al. (2014) concurrently with this work.

We describe our observations and data reduction in Section 2 and present our observational results in Section 3. We use the data in Section 4 to constrain the merger configuration, which is critical to interpreting the observed gas motion. Section 5 presents our two-outflow model for the observed velocity structure and gas distribution. The outflow from the southern nucleus has remarkable velocity distribution, collimation, and energy. We discuss the driving mechanism in Section 6. Section 7 compares our findings in NGC 3256 with similar phenomena in other galaxies and Section 8 summarizes our conclusions.

2. OBSERVATIONS

2.1. *ALMA*

Our ALMA observations in Cycle 0 were made in 2011–2012 using up to twenty-three 12 m diameter antennas, as summarized in Table 2. We observed in the 3 mm band (Band 3) and the 0.85 mm band (Band 7), each in two array configurations jointly covering projected baselines between 15 m and about 370 m. The Band 3 observations were for a single pointing at a position between the two nuclei. The primary beam of the ALMA 12 m antennas has a full width at half maximum (FWHM) of 53″ at the frequency of the redshifted CO(1–0) line.[7] In Band 7 we made a seven-point hexagonal mosaic with the same central position and a $7\overset{''}{.}3$ spacing between adjacent pointings. The FWHM of the primary beam is 18″ and that of the mosaicked sensitivity pattern is about 25″ for the redshifted CO(3–2) line. We used a correlator setup having 0.488 MHz channel spacing and about 3.5 GHz continuous coverage in each sideband.

With our Band 3 data, we combined an earlier ALMA data set obtained through the Commissioning and Science Verification (CSV) program carried out by the Joint ALMA Observatory. The CSV observations, also listed in Table 2, had about the same on-source integration time (three hours) as our Cycle 0

[7] The FWHM size of the primary beam is assumed to be $1.17(\lambda/12)$ for ALMA and $1.15(\lambda/6)$ for SMA, where λ is the wavelength in meters.

Table 2
Log of ALMA Observations

ID (1)	UT Date (2)	Config. (3)	N_{ant} (4)	BL Range (m) (5)	$\langle T_{sys}\rangle$ (K) (6)	S_{gain} (Jy) (7)	α_{gain} (8)	α_{bp} (9)	T_{gal} (minutes) (10)
Band 3:									
B3-c1	2011 Apr 16	CSV	7	12–90	66	1.94	−0.25	−0.25	90
B3-c2	2011 Apr 17	CSV	8	14–89	61	1.94	−0.25	−0.25	90
B3-1	2011 Dec 29	COM	14	16–259	74	1.35	−0.50	−0.34	31
B3-2	2011 Dec 30	COM	13	15–253	72	1.35	−0.50	−0.34	31
B3-3	2012 Jan 27	COM	17	17–269	72	1.33	−0.67	−0.336	34
B3-4	2012 Jan 27	COM	17	17–264	69	1.33	−0.67	−0.336	34
B3-5	2012 Mar 27	EXT	14	20–374	64	1.49	−0.56	−0.43	34
B3-6	2012 Jul 28	EXT	23	16–364	78	1.46	−0.68	−0.67	29
Band 7:									
B7-1	2012 Jan 24	COM	16	15–256	181	0.54	−1.03	−0.61	30
B7-2	2012 May 21	EXT	14	16–360	186	0.75	−1.18	−0.67	30
B7-3	2012 Jun 4	EXT	20	16–360	149	0.67	−0.89	−0.86	30

Notes. (2) Date of observations. (3) ALMA array configuration. Cycle 0 had two configurations, COM=compact and EXT=extended. (4) Number of useable antennas after flagging bad data. Some of them are partly flagged. (5) The range of projected baselines toward NGC 3256. (6) Median single-side-band system temperature toward NGC 3256. (7)–(8) Flux density and spectral index of the gain calibrator, J1037−295 in the CSV observations and J1107−448 in our Cycle 0 observations. The flux densities in Band 3 are the ones at 100 GHz and those in Band 7 are at 348 GHz. Primary flux calibrator was Mars or Titan. (9) Spectral index of the bandpass calibrator, J1037−295 and 3C279 in the CSV and Cycle 0 observations, respectively. (10) Total integration time on NGC 3256. The calibration parameters (7)–(9) for the data B3-c2 are taken from the measurements in B3-c1. Those for B3-1 and B3-2 as well as B3-3 and B3-4 are respectively from combined fitting of the two calibration data sets.

Table 3
Frequency Coverage

Obs. (1)	Band (2)	SB (3)	f(LSRK) (GHz) (4)	f_{rest} (GHz) (5)
Cycle 0	B7	U	352.220–355.619	355.511–358.941
Cycle 0	B7	L	340.226–343.629	343.405–346.839
CSV	B3	U	111.693–115.110	112.737–116.185
Cycle 0	B3	U	111.598–114.962	112.641–116.036
CSV	B3	L	99.622–102.823	100.553–103.784
Cycle 0	B3	L	99.606–102.910	100.537–103.871

Notes. (3) U = upper sideband (USB), L = lower sideband (LSB). (4) The range of LSRK frequencies covered in all executions for a source in the direction of NGC 3256. The CSV data has a ∼0.1 GHz gap in the middle of USB. The execution B7-2 in Table 2 does not have the upper half of the USB. (5) The frequency coverage in the rest frame of NGC 3256 at V(radio, LSRK) = 2775 km s^{-1}.

observations, albeit with seven or eight antennas. They provide dense sampling of short projected baselines between 12 m and 90 m. The CSV observations were made toward a slightly offset position (4″.2 from our Cycle 0 observations) with a correlator setup of 15.6 MHz channel spacing and with almost the same frequency coverage as our Cycle 0 observations (Table 3). The CSV and Cycle 0 data were combined as a mosaic because of the pointing offset.

All ALMA data were calibrated from the raw data[8] in a uniform manner using the CASA[9] reduction package versions 4.0 and 4.1. Most notably, we used the "Butler-JPL-Horizons 2012" model for Titan and Mars in our flux calibration, measured and accounted for the spectral slopes of our bandpass and gain calibrators in our calibration, and checked the flatness of our spectral bandpass by looking at the spectrum of the gain calibrator after all calibrations. Data showing non-linear baselines were flagged.[10]

Imaging and basic data analysis were also made in CASA. For lines, we binned our data to spectral resolutions of 4, 10, and 20 MHz for Cycle 0 Band 3; 15.6 MHz for the combined CSV + Cycle 0 data in Band 3; and 10 and 30 MHz for Band 7. Table 4 lists the six lines detected in our ALMA data, as well as two notable non-detections. After carefully inspecting the full widths of these lines, we made continuum data by summing up line-free channels. The continuum has been subtracted from our line data in the u–v domain for the CSV + Cycle 0 data and in the image domain for the rest. This is because we are most interested in weak- and broad-line emission near the phase center in the former data set, while we desire better subtraction across the imaging area for other data sets.

Parameters of our reduced data are summarized in Tables 5 and 6. Compared to our previous SMA observations, the new ALMA observations improved spatial resolution by about a factor of three and sensitivity in line-brightness temperature by about an order of magnitude. Our CO(1–0) data cubes made from the Cycle 0 data alone recovered 76%–87% of the single-dish flux measured with a 43″ beam (FWHM) by

[8] In ALMA Science Data Model format.

[9] Common Astronomy Software Applications (McMullin et al. 2007).

[10] The versions of CASA that we used do not allow the flagging of only one of the two linear polarizations on individual baselines because the two polarizations share a flagging variable in the data structure. Therefore, when one of the two linear polarizations on a baseline was found faulty the remaining one was copied over the corrupted one and both the original and copied visibilities were down-weighted to conserve the net weights of the rescued data.

Table 4
Lines Imaged toward NGC 3256

Species, Transition (1)	f_{rest} (GHz) (2)	E_u/k (K) (3)	Note (4)
HCO^+(J = 4–3)	356.7342	42.8	B7 USB
CO(J = 3–2)	345.7960	33.2	B7 LSB
CO(J = 2–1)	230.5380	16.6	SMA USB
^{13}CO(J = 2–1)	220.3987	15.9	SMA LSB
CO(J = 1–0)	115.2712	5.5	B3 USB
CN(N = 1–0; J = 3/2–1/2)	113.4949	5.4	B3 USB
CN(N = 1–0; J = 1/2–1/2)	113.1688	5.4	B3 USB
CH_3CCH($J_K = 6_0$–5_0)	102.5480	17.2	B3 LSB
Non-detections:			
HCO^+(v_2 = 1, J = 4–3, l = 1f)	358.2424	1236.7	B7 USB
HCN(v_2 = 1, J = 4–3, l = 1f)	356.2556	1067.1	B7 USB

Notes. The data are taken from splatalogue. (2) Rest frequency. For CN the f_{rest} frequencies are mean values of five and four transitions (of almost identical E_u), respectively, for the one group at around 113.4949 GHz and the other at around 113.1688 GHz. The ranges of f_{rest} in each group are 32 and 68 MHz, respectively, for the first and the second group. CH_3CCH (propyne or methyl acetylene) is a symmetric top molecule and has several transitions around this frequency with different E_u for different K. Listed above is the one with $K = 0$ involving the lowest E_u. Intensity-weighted mean frequency can be several MHz lower than this for excitation temperatures on the order of 50 K. (3) The upper level energy divided by the Boltzmann constant.

Aalto et al. (1995). The fraction is highest in the data cube made with lower weights to longer baselines. We recovered 91%–97% of the single-dish CO(1–0) flux in the cubes made from the CSV + Cycle 0 data. Similarly, the ratio of CN(N = 1–0; J = 3/2–1/2) line flux in our observations to the 46″ beam measurement by Aalto et al. (2002) ranges from 0.78 to 1.14; the former is for the ∼1″.5 resolution cube made with the Cycle 0 data alone and the latter is for the ∼5″.5 resolution cube made from the CSV + Cycle 0 data. We expect similar recovery rates for other Band 3 lines and continuum, but the recovery rate will be lower for CO(3–2) in Band 7 because the central hole in the u–v plane is larger. For HCO^+(4–3) in Band 7, our data cubes made with natural weighting recovered 93%–107% of the single-dish flux measured in a 17″ beam (FWHM) by Zhang et al. (2014). This high fraction suggests that this line is intrinsically less extended than CO, probably because it traces dense molecular gas.

2.2. SMA

We added new data taken in 2008 to our SMA 1.3 mm observations reported in SHP06, increasing the maximum projected baseline from 179 m to 509 m and doubling the total on-source time from 6.9 hr to 12.9 hr. The new observations in two nights had seven antennas and excellent weather with 220 GHz zenith opacity between 0.04 and 0.06. We observed the same position as in our previous observations (as well as our ALMA observations) using the tuning for the same three J = 2–1 lines as before, namely ^{12}CO, ^{13}CO, and $C^{18}O$ although only the first two were bright enough for imaging at high angular resolutions. The primary beam of the SMA 6 m antennas has a FWHM size of 52″ for the redshifted CO(2–1) line. The data were reduced with the same steps as before using the MIR reduction package.

2.3. Conventions

The offset coordinates in this paper relate to our SMA and ALMA Cycle 0 phase-tracking center in Table 1. We adopt

Table 5
Continuum Data Properties

Source	Band	SB	wt.	Beam ($''$, $''$)	rms (mJy beam^{-1})	max	rms (mK)	max	Figure
(1)	(2)	(3)	(4)	(5)	(6)	(7)	(8)	(9)	(10)
Cyc0	B7	D	br	0.52 × 0.36	0.16	4.42	8.6	237	1(c), 10(b), 16
Cyc0	B7	D	na	0.65 × 0.49	0.13	5.80	4.1	183	1(b)
Cyc0	B7	U	na	0.63 × 0.48	0.17	5.76	5.5	185	
Cyc0	B7	L	na	0.67 × 0.50	0.15	5.71	4.7	179	
Cyc0	B7	D	tp	1.19 × 1.11	0.24	14.21	1.8	108	10(a)
CSV + Cyc0	B3	D	na	2.77 × 2.36	0.017	5.09	0.28	84	1(a)
CSV + Cyc0	B3	U	na	2.63 × 2.40	0.037	5.00	0.56	75	
CSV + Cyc0	B3	L	na	2.81 × 2.35	0.018	5.13	0.32	91	

Notes. (1) Cyc0 = ALMA Cycle 0, CSV + Cyc0 = ALMA CSV and Cycle 0 combined. (3) Sideband. D = DSB, U = USB, L = LSB. (4) Visibility weighting for imaging. br = Briggs with `robust = 0`, na = natural, tp = tapered. (5) Size of the synthesized beam in FWHM. (6)–(7) rms noise and maximum in the continuum image in the unit of mJy beam^{-1}. These are measured before correction for the primary-beam attenuation. (8)–(9) The same rms noise and maximum in the unit of milli-kelvin.

Table 6
Line Data Properties

Source	Line	wt.	δV (km s^{-1})	Beam ($'' \times ''$)	rms (mJy beam^{-1})	max	rms (mK)	max (K)	Figure
(1)	(2)	(3)	(4)	(5)	(6)	(7)	(8)	(9)	(10)
Cyc0	HCO^+(4–3)	na	25.2	0.65 × 0.49	1.53	42.9	47	1.3	6, 12
Cyc0	HCO^+(4–3)	na	8.4	0.65 × 0.49	2.55	46.5	78	1.4	3
Cyc0	CO(3–2)	br	26.0	0.58 × 0.39	1.92	470.9	88	21.7	5
Cyc0	CO(3–2)	na	26.0	0.68 × 0.50	1.20	624.2	37	19.0	12
Cyc0	CO(3–2)	tp	26.0	1.20 × 1.10	1.67	1725.7	13	13.6	14
Cyc0	CO(3–2)	br	8.7	0.58 × 0.39	3.31	479.2	152	22.1	2, 7, 10, 15, 16
Cyc0	CO(3–2)	tp	8.7	1.20 × 1.10	2.48	1777.3	20	14.0	10, 13
SMA	CO(2–1)	na	10.0	1.03 × 0.56	13.0	480.0	526	19.4	2
SMA	^{13}CO(2–1)	tp	20.0	2.14 × 1.69	14.1	138.5	100	0.98	3
Cyc0	CO(1–0)	br	10.4	1.61 × 1.24	1.46	321.2	69	15.1	2
Cyc0	CO(1–0)	na	10.4	2.32 × 2.06	0.96	589.8	19	11.6	15
Cyc0	CN(1–0, 3/2–1/2)	br	26.4	1.69 × 1.28	0.72	26.6	32	1.19	3, 19
Cyc0	CN(1–0, 1/2–1/2)	br	26.5	1.69 × 1.28	0.72	12.5	33	0.56	3, 19
Cyc0	CH_3CCH(6–5)	na	29.2	2.62 × 2.14	0.34	3.7	7.2	0.078	3, 20
CSV + Cyc0	CO(1–0)	br	40.6	1.69 × 1.31	0.69	314.9	29	13.3	4
CSV + Cyc0	CO(1–0)	na	40.6	2.92 × 2.57	0.43	736.6	5.4	9.2	11, 14
CSV + Cyc0	CO(1–0)	tp	40.6	5.78 × 5.17	0.52	1732.2	1.6	5.4	8, 11, 12
CSV + Cyc0	CN(1–0, 3/2–1/2)	tp	41.3	5.90 × 5.16	0.41	87.4	1.3	0.28	9, 12

Notes. (1) Cyc0 = ALMA Cycle 0, CSV + Cyc0 = ALMA CSV and Cycle 0 combined. (2) Emission line. See Table 4 for more line information. (3) Visibility weighting for imaging. br = Briggs with `robust = 0`, na = natural, tp = tapered. (4) Velocity resolution for the line. (5) Size of the synthesized beam in FWHM. (6)–(7) rms noise and maximum in the channel maps in the unit of mJy beam^{-1}. These are measured before correction for the primary-beam attenuation. (8)–(9) The same rms noise and maximum in brightness temperature.

radio positions for the two merger nuclei: R.A. = $10^h27^m51\overset{s}{.}23$, decl. = $-43°54'14\overset{''}{.}0$ (J2000) for the northern (N) nucleus; and R.A. = $10^h27^m51\overset{s}{.}22$, decl. = $-43°54'19\overset{''}{.}2$ (J2000) for the southern (S) nucleus (Neff et al. 2003). Our phase tracking center is the midpoint of these nuclei with the last R.A. digit rounded up. We use radio-defined velocity with respect to the local standard of rest (LSR) throughout this paper (LSRK in the ALMA terminology). We adopt 2775 km s^{-1} (radio, LSR) for the systemic velocity of the galaxy and measure offset velocities from this V_{sys} (e.g., in presenting channels maps). Our previous SMA observations found this to be a good fiducial velocity not only for the whole system, but also for individual nuclei because they almost align on the kinematic minor axis of the merger (SHP06). The noise in Tables 5 and 6, and elsewhere in this paper, are (based on) thermal noise measured in emission-free channels or, for continuum, in areas far from a strong signal. Actual noise is probably higher near strong emissions because the data quality there is limited by the dynamic range.

3. OBSERVATIONAL RESULTS

3.1. Continuum

The 3 mm continuum emission shown in Figure 1(a) peaks at the two nuclei and extends to a radius of at least 20$''$ (3 kpc) with arcs and arm-like features in the region. Continuum emission at 1.3 mm also peaks at the two nuclei (SHP06). The nuclear peaks and the extended emission at 3 mm are morphologically similar to those previously observed at 6 and 3.6 cm (Norris & Forbes 1995; Neff et al. 2003, in their Figure 1). Both nuclei are resolved in our 0.86 mm continuum images in Figures 1(b) and (c).

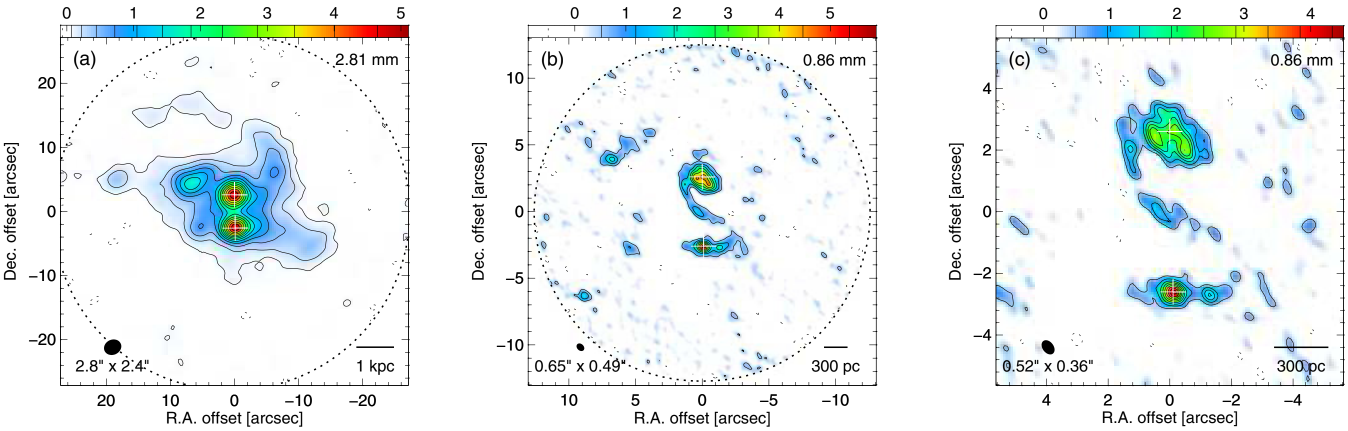

Figure 1. NGC 3256 continuum at λ ∼ 2.8 mm (left) and 0.86 mm (middle and right). The two plus signs are at the positions of the cm-wave radio nuclei in Neff et al. (2003). They have a separation of 5″ = 850 pc on the sky and serve as a reference for the zoom factor of the images. The offset coordinates are measured from the ALMA Cycle 0 pointing position in Table 1. The maps are corrected for the attenuation of the (mosaicked) primary beam responses and are truncated at the 50% of their peaks. The nth contours are at $\pm 4n^{1.7}\sigma$, $\pm 4n^{1.2}\sigma$, and $\pm 3n\sigma$ in Panels (a), (b), and (c), respectively, with zero contours omitted and negative contours dashed. The rms noise σ are the ones measured before the primary-beam correction and are given in Table 5. The intensity unit of the color bars at the top is mJy beam^{-1}. The peaks in Panels (a), (b), and (c) are 5.1 (0.08), 5.9 (0.19), and 4.5 (0.24) mJy beam^{-1} (K), respectively.

(A color version of this figure is available in the online journal.)

The northern nucleus has a high-intensity plateau with a diameter of about 2″ (0.3 kpc). The southern nucleus has a compact (∼0.″5, 80 pc) peak with a linear feature elongated by about 3″ (0.5 kpc) in the east–west direction through the nucleus. The extent of the northern nucleus agrees with that in X-rays (FWHM ∼1.″5 in 0.5–10 keV measured by Lira et al. 2002). Our highest-resolution continuum image in Figure 1(c) hints at a (broken) ring in the plateau around the northern nucleus. It is comparable in size to an optical ring-like structure noted by Laine et al. (2003). There is also conspicuous bridge-like emission between the two nuclei that emanates from the circumnuclear region of the northern nucleus and curves toward the western side of the elongated continuum emission across the southern nucleus. The peak brightness temperatures in Figure 1 are between 0.08 and 0.24 K. The compact southern nucleus shows a higher peak T_{b} than the northern nucleus when the northern circumnuclear plateau is spatially resolved.

We measured the spectral slope of the continuum emission at 2.8 mm and 0.86 mm by comparing the data in the upper and lower sidebands separated from each other by about 12 GHz. For this, we used single-sideband continuum images that have a common spatial resolution and a common range of u–v baseline lengths, flagging the shortest baselines in the lower sideband (LSB) and the longest in the upper sideband (USB). Unfortunately, we cannot reliably compare the 2.8 mm and 0.86 mm data to estimate the spectral index between them because the difference in their u–v coverages is too large. The spectral index α of the continuum emission (for $S_\nu \propto \nu^\alpha$ where ν is frequency and S_ν is flux density) is found to be −0.1 at 2.8 mm and +3 at 0.86 mm in the central 20″. The spectral indices at the individual nuclei are also measured and listed in Table 7. The index α changes its sign between negative at 2.8 mm and positive at 0.86 mm, also at the nuclei. Such a spectral energy distribution (SED) must have a local minimum between the two wavelengths. This can be attributed to different emission mechanisms dominant above and below ∼1–2 mm. At shorter wavelengths, thermal dust continuum usually dominates with $\alpha \approx 3$–4 due to the dust mass opacity coefficient having a power law index of 1–2. At longer wavelengths, continuum is usually from a combination of free–free emission with $\alpha \sim -0.1$ from thermal electrons and synchrotron emission with $\alpha \sim -1$ (±0.5). We found that α is larger at the northern nucleus than at the southern nucleus at 0.86 mm and 2.8 mm. The smaller α of the southern nucleus suggests that it has a larger fraction of free–free or synchrotron emission and less of dust thermal emission than the northern nucleus.

Table 7
Continuum Flux Densities and Spectral Indices

Band (1)	SB (2)	ν_{mean} (GHz) (3)	S_ν(20″) (mJy) (4)	S_ν(N) (mJy) (5)	S_ν(S) (mJy) (6)	θ (″) (7)	α(20″) (8)	α(N) (9)	α(S) (10)
B7	U	354.236	122.2	13.2	9.6	1	+3.00	+3.72	+1.56
B7	L	341.203	109.2	11.5	9.1	1	⋯	⋯	⋯
B3	U	113.313	28.4	5.1	5.0	2.7	−0.10	−0.12	−0.19
B3	L	101.222	28.8	5.2	5.1	2.7	⋯	⋯	⋯

Notes. (2) U = USB, L = LSB. (3) Mean frequency of the single sideband continuum. (4) Flux density of the continuum emission integrated over a 20″ diameter aperture centered at the midpoint of the two nuclei. Only the Cycle 0 data are used. (5)–(6) Flux densities at the radio positions of the northern and southern nuclei, respectively, within the Gaussian beams whose FWHM sizes are in (7). Data in Columns (4), (5), and (6) are corrected for the primary beam responses but not for any missing flux. More digits are shown than allowed for their absolute accuracies because the ratio between USB and LSB are free from the common sources of error for the two sidebands. (8)–(10) Spectral indices for the 20″ aperture, northern nucleus, and southern nucleus calculated between the USB and LSB of each receiver band.

3.2. Line

Line maps are shown in Figures 2 and 3 for the eight lines that we imaged. Shown here are the integrated intensity, intensity-weighted mean velocity, intensity-weighted velocity dispersion, and peak brightness temperature. Line channel maps are shown in Figures 4–6 and in Figures 19 and 20 in the Appendix for weak lines. We display low-velocity resolutions for space reasons, although we also made and analyzed data cubes with higher velocity resolutions. Note that contour levels are different between channels with and without strong signals in the CO channel maps. This is to display both faint high-velocity

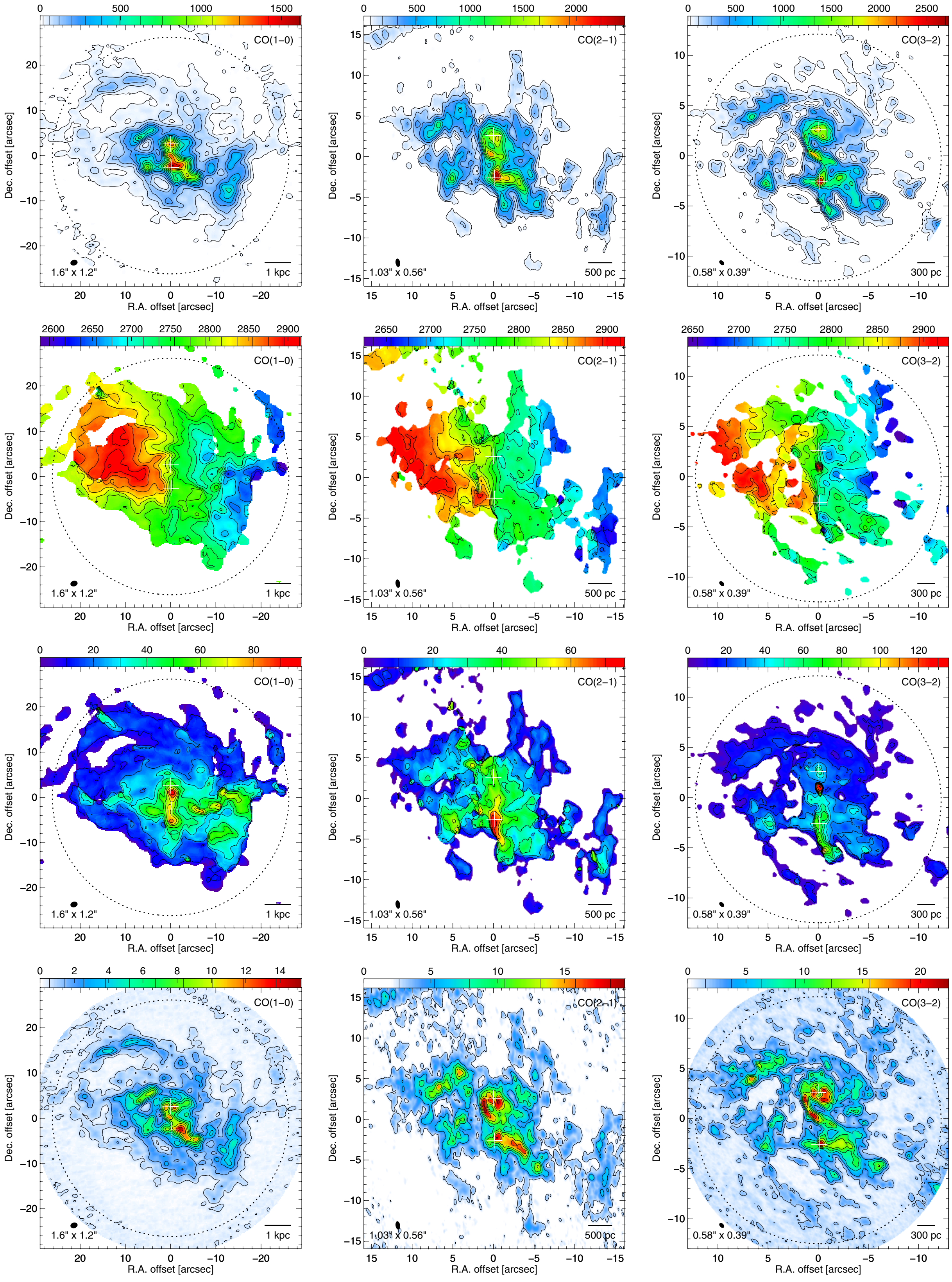

Figure 2. ^{12}CO($J = 1$–0) (left), ^{12}CO($J = 2$–1) (middle), and ^{12}CO($J = 3$–2) (right) images of NGC 3256. The four rows are, from the top, moment 0, 1, 2 maps and peak $T_{\rm b}$ maps with the data units of K km s^{-1}, km s^{-1}, km s^{-1}, and K, respectively. The two plus signs are at the positions of the cm-wave radio nuclei. They have a separation of $5'' = 850$ pc on the sky and serve as a reference for the zoom factor of the images. The offset coordinates are measured from the common ALMA Cycle 0 and SMA pointing position in Table 1. Intensity maps (the top and the bottom rows) are corrected for the (mosaicked) primary beam responses; dotted lines show them at 50% of their peaks. The nth contours in the moment 0 maps are at cn^p K km s^{-1}, where $(c, p) = (18, 1.7)$, $(61, 1.5)$, and $(27, 2)$ for CO(1–0), (2–1), (3–2), respectively. The moment 1 maps have contours at every 20 km s^{-1} including 2775 km s^{-1} and the moment 2 maps at every 10 km s^{-1} starting from 10 km s^{-1}. The nth contours in the peak $T_{\rm b}$ maps are at dn^q K, where $(d, q) = (0.55, 1.4)$, $(2.5, 1.0)$, and $(1.5, 1.3)$ for CO(1–0), (2–1), (3–2), respectively. The maximum brightness temperatures in the maps are 15.2, 19.5, and 22.4 K for CO(1–0), (2–1), (3–2), respectively. Synthesized beams are shown with their FWHM sizes at the bottom-left corners of the panels.

(A color version of this figure is available in the online journal.)

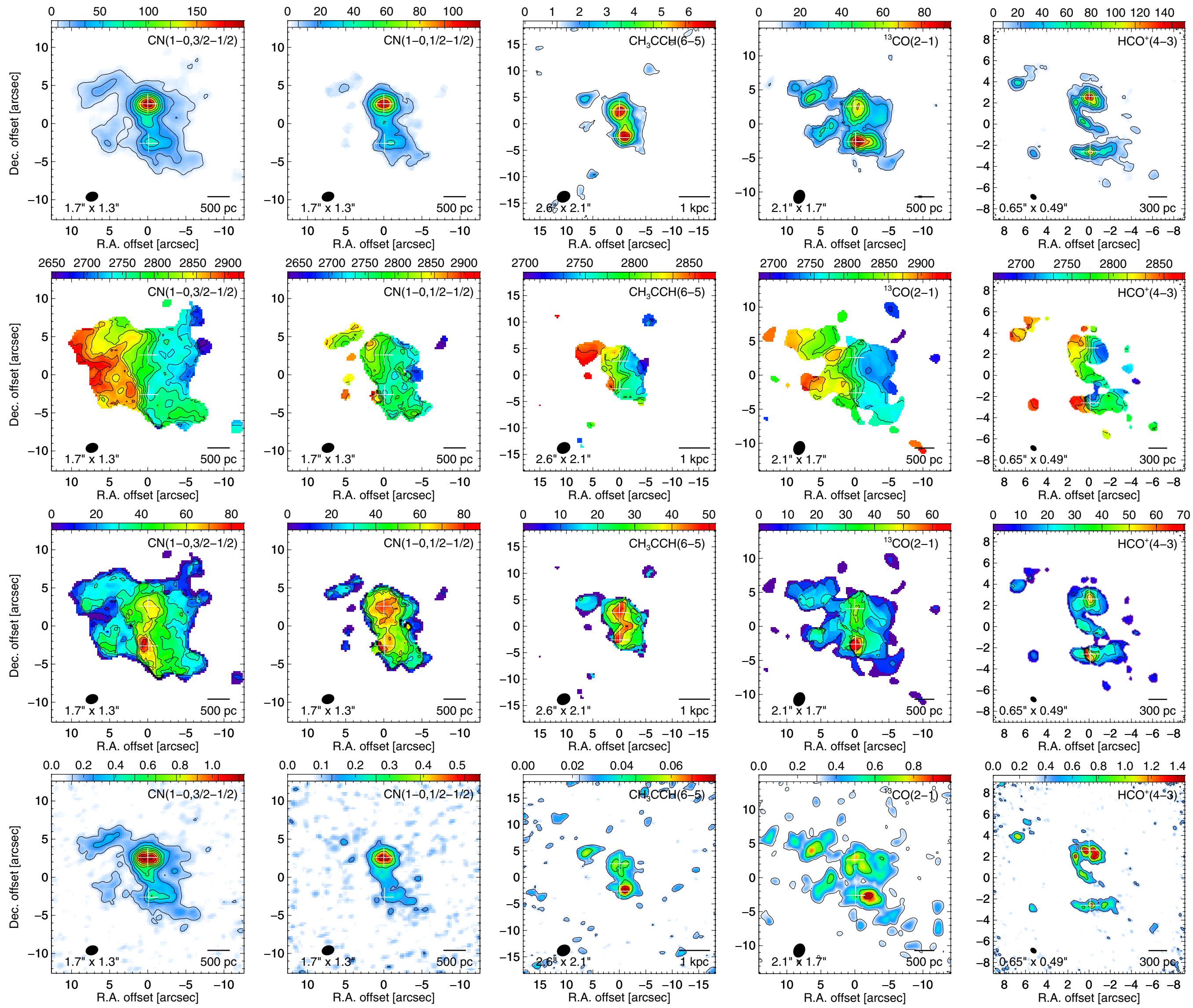

Figure 3. Molecular line maps of NGC 3256. The lines are, from left to right, CN(N = 1–0; J = 3/2–1/2), CN(N = 1–0; J = 1/2–1/2), CH_3CCH(J = 6–5), ^{13}CO(J = 2–1), and HCO^+(J = 4–3). The four rows are, from the top to the bottom, the moment 0, 1, 2 maps and peak T_b map in units of K km s^{-1}, km s^{-1}, km s^{-1}, and K, respectively. Intensity maps at the top and the bottom rows are corrected for the sensitivity patterns of the primary beams; all plots are within 50% of their peaks. The nth contours are at cn^p K km s^{-1} in the moment 0 maps and dn^q K in the peak T_b maps with (c, p) = (6.6, 1.5), (6.5, 1.5), (1.2, 1), (11.2, 1) and (7.9, 1.5) and (d, q) = (0.13, 1), (0.13, 1), (0.023, 1), (0.30, 1) and (0.39, 1), respectively, from the left-most column to right. The moment 1 maps have contours at every 20 km s^{-1} including 2775 km s^{-1} and the moment 2 maps at every 10 km s^{-1} starting from 10 km s^{-1}.

(A color version of this figure is available in the online journal.)

emission and strong emission near the systemic velocity. Also for space reasons, analysis of these line data beyond the context of this paper (i.e., overview and outflows) will be reported elsewhere.

3.2.1. Spatial Distribution

All the molecular lines have emission peaks at or near the two nuclei, as does the continuum emission. The degree of concentration and the relative strengths of the two nuclei vary among the lines. The bridge-like feature between the northern and southern nuclei is also visible in line emission, most clearly in CO(2–1), CO(3–2), and HCO^+(4–3) integrated intensity images. There are additional arc features seen in the continuum and/or line data. The near-linear feature crossing the southern nucleus in the east-west direction is also visible in line emission, most clearly in CO(3–2) and HCO^+(4–3).

3.2.2. Velocity Field

Large scale. The CO(1–0) velocity map in Figure 2 shows overall rotation in the central ∼5 kpc with the receding major axis at position angle (p.a.) ∼ 70°. Significant deviations from circular motion at this scale are visible mostly at the locations of the arm-like features. The apparent kinematic major axis is at p.a. ∼ 90° within about 1 kpc of the nuclei. Therefore both nuclei line up with the apparent kinematic minor axis at this scale, for example, as seen in the first moment maps of CO(1–0), CO(2–1), and CN(1–0). These large scale kinematics of molecular gas are consistent with those in SHP06.

N nucleus. Our data show gas rotation around the northern nucleus within about a 300 pc radius. This appears as a butterfly-like pattern of isovelocity contours in the mean velocity maps of HCO^+(4–3) (Figure 3) and CO(3–2) (Figure 7(b)), the latter

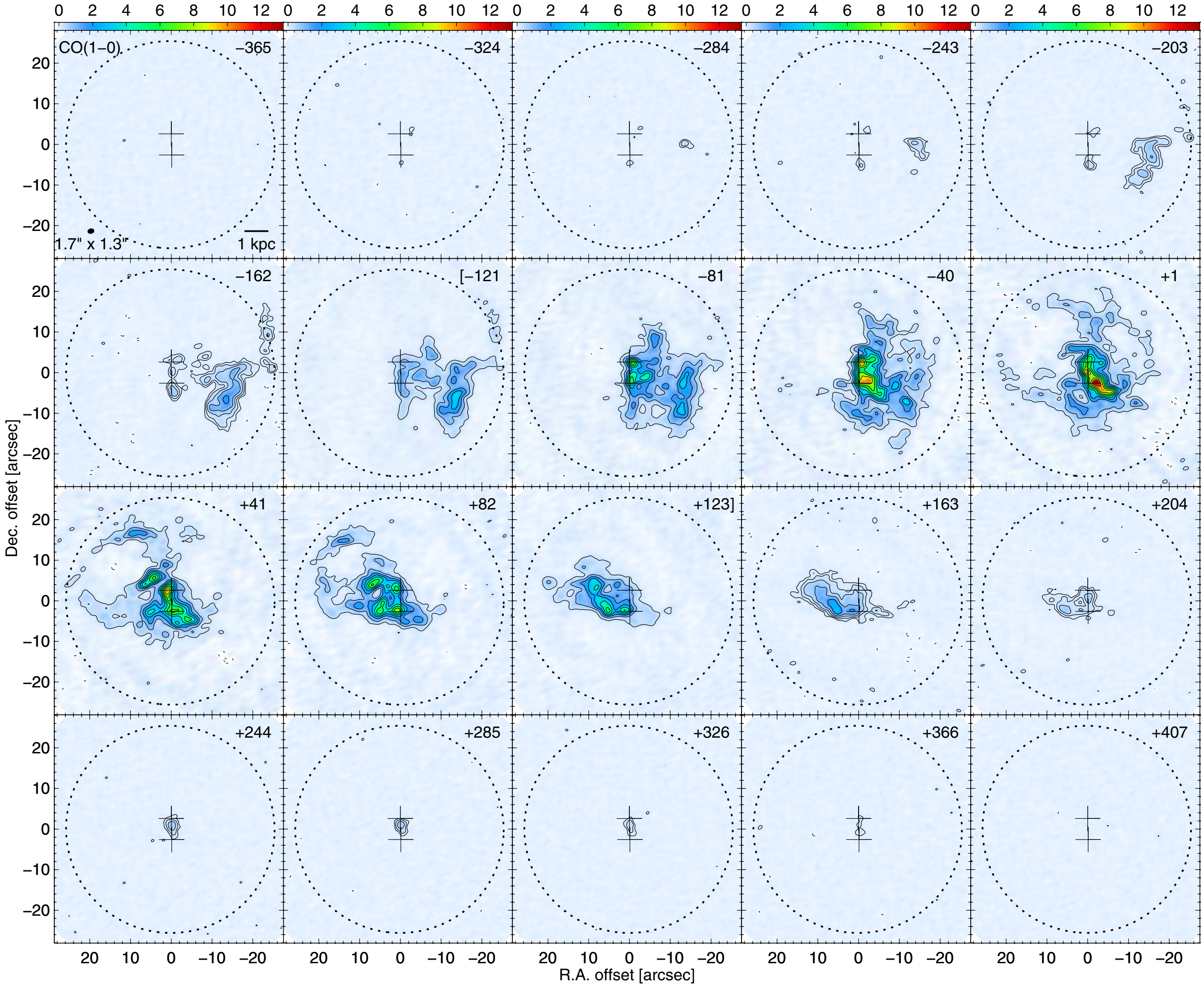

Figure 4. CO(1–0) channel maps. Offsets from 2775 km s^{-1} are at the top-right corners. Contours are at $\pm 7n^{1.8}\sigma$ ($n = 1, 2, 3, \cdots$) in channels from −121 to +123 km s^{-1}, whose maxima exceed 100σ, and at $\pm 3.5 \times 2^{m}\sigma$ ($m = 0, 1, 2, \cdots$) in the other channels. Square brackets attached to the velocity labels indicate the former velocity range. The rms noise is $\sigma = 29$ mK. Negative contours are dashed. This plot is not corrected for the primary-beam response, whose 50% contours are the dotted circles. The peak intensity of CO(1–0) is 13.3 K in this plot. The two plus signs in each panel are at the two nuclei. The black ellipse in the top-left panel shows the FWHM size of the observing beam.

(A color version of this figure is available in the online journal.)

of which was made only with brighter circumnuclear emission. We fitted the velocity field to obtain the kinematic major axis at p.a. ≈ 75° and the disk inclination of $i \approx 30°$ for a region with a 3″ major axis diameter. This kinematic major axis agrees reasonably well with the morphological major axis of the circumnuclear high-intensity region of the northern nucleus in CO, HCO^+, and 0.86 mm continuum. The kinematic major axis gradually changes its position angle, so that it is about 60° at larger radii and about 90° closer to the nucleus. This may be due to a warp of the northern nuclear disk or non-circular motions of the gas in the disk.

S nucleus. In the mean velocity maps, the southern nucleus has in its vicinity a velocity gradient in the east–west direction (p.a. ≈ 90°). The isovelocity contours, however, do not show a clear butterfly pattern there. The largest mean velocity gradient is at about 0.″5 east of the southern radio nucleus (white plus sign), while line integrated intensity tends to peak slightly west or northwest of the nucleus (e.g., in CO, ^{13}CO, CN, but not in HCO^+), by about 0.″3–0.″5.

Between the nuclei. Conspicuously, the most redshifted CO(3–2) emission is about 2″ south of the northern nucleus in the CO(3–2) mean velocity map in Figure 2. This is due to the high-velocity wing of CO emission and is the reason for the very large line width at the same location in the CO(3–2) line-width map. This feature does not show up in Figure 7(b) because the faint wing emission is below the cutoff used for the moment map. The high-velocity emission is separately described in Section 3.3 along with the line width information in Figures 2 and 3.

3.2.3. Peak T_b and Integrated Intensity

The three ^{12}CO lines have peak integrated intensities on the order of 2×10^3 K km s^{-1} and maximum brightness

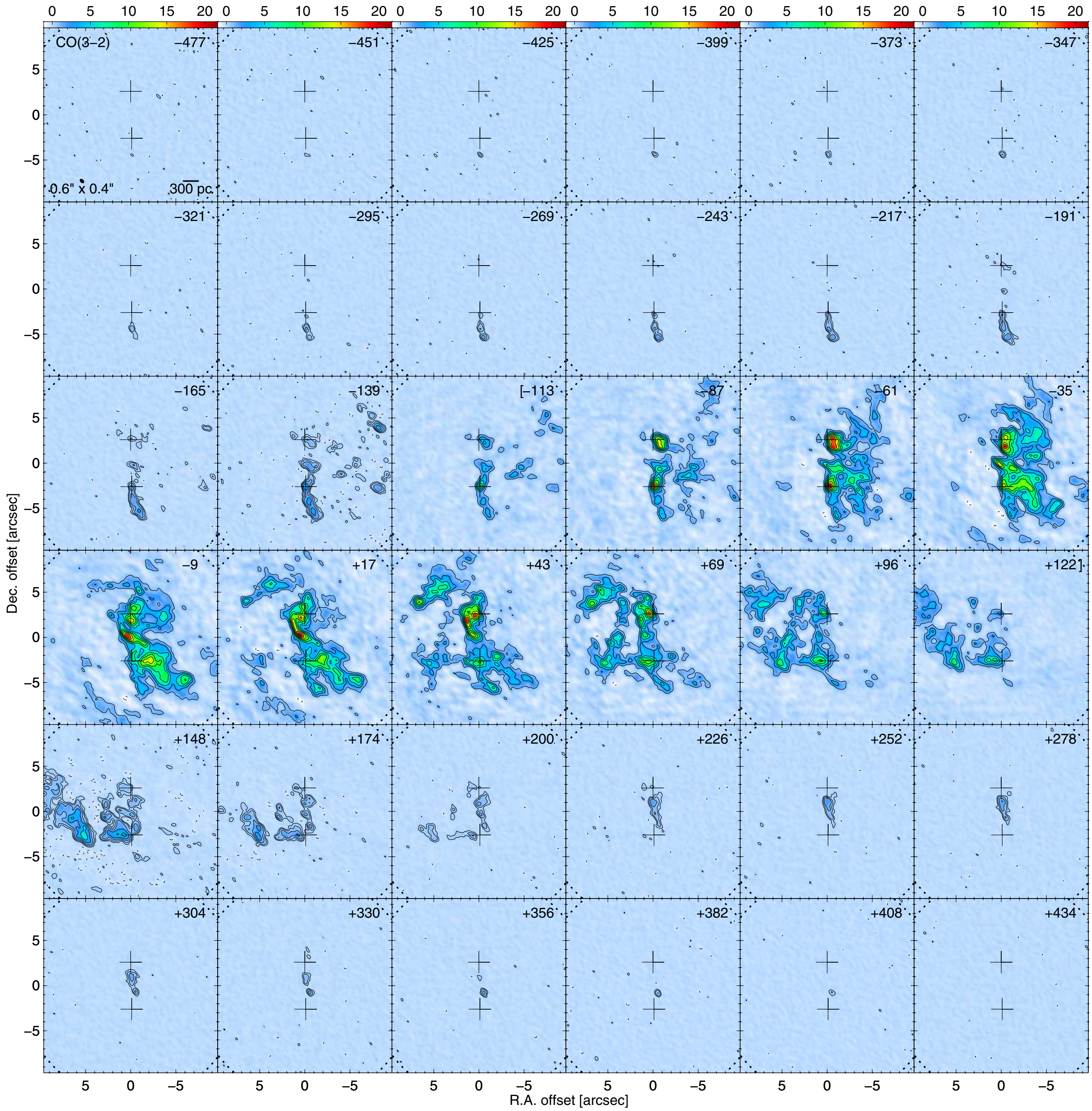

Figure 5. CO(3–2) channel maps. Offsets from 2775 km s^{-1} are at the top-right corners of individual panels. Contours are at $\pm 10n^{1.5}\sigma$ ($n = 1, 2, 3, \cdots$) in channels from -113 to $+122$ km s^{-1}, whose maxima exceed 100σ, and at $[-6, -3, 3, 6, 12, 24, 48, 96]\sigma$ in the rest. Square brackets attached to the velocity labels indicate the former velocity range. The rms noise is $\sigma = 88$ mK. Negative contours are dashed. The data are not corrected for the mosaicked primary-beam response, whose 50% contours are the dotted circles (visible only at the corners). The peak intensity of the line is 21.7 K in this plot whereas that of the 0.88 mm continuum already subtracted here is 0.22 K at this resolution. The two plus signs in each panel show the locations of the two nuclei. The black ellipse in a corner of the first panel shows the FWHM size of the observing beam.

(A color version of this figure is available in the online journal.)

temperatures of about 20 K, both at about 1″ resolution. The maxima are 22.4 K and 2730 K km s^{-1} in CO(3–2) at our highest resolution ($0''.58 \times 0''.39 \approx 80$ pc). The peaks of line emission are in the vicinity of the two nuclei, in the spiral feature running between the two nuclei, and in the linear feature across the western nucleus, particularly in its western side. At least for these regions, our data show neither significant decline of (integrated) intensity in higher transitions, which would suggest significant subthermal excitation, nor significant increase in (integrated) intensity, which would indicate optically thin emission of thermalized warm molecular gas.

Other lines are much weaker than the ^{12}CO lines, having peak brightness temperatures at about 1 K or lower. Possible reasons for this weakness include that these lines are optically thin,

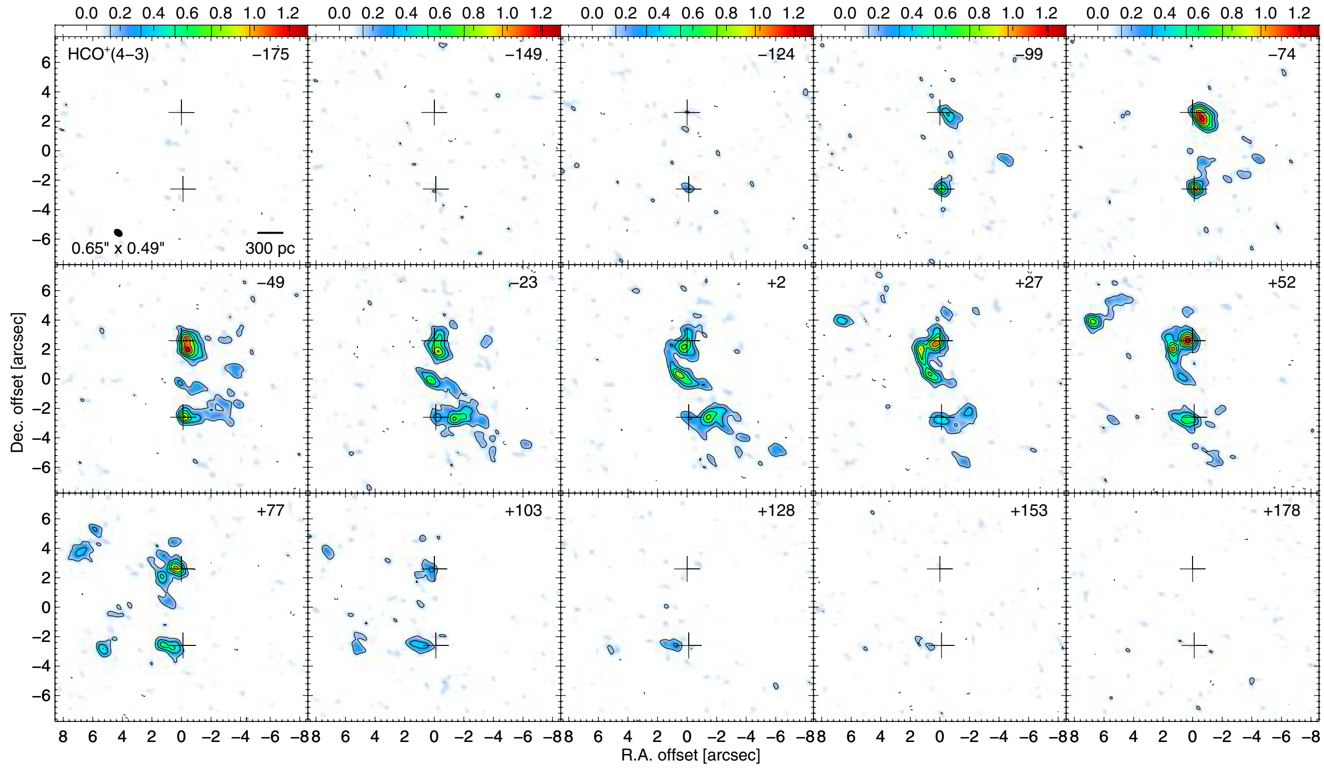

Figure 6. HCO$^+$(4–3) channel maps. Offsets from 2775 km s^{-1} are at the top-right corners. Contours are at $\pm 3n^{1.2}\sigma$ ($n = 1, 2, 3, \cdots$), where the rms noise is $\sigma = 47$ mK. Negative contours are dashed. The data are not corrected for the mosaicked primary-beam response, whose FWHM is about 24 arcsec. The peak line intensity is 1.3 K in this plot. The two plus signs in each panel are at the two nuclei. A black ellipse in the first panel shows the FWHM size of the observing beam.

(A color version of this figure is available in the online journal.)

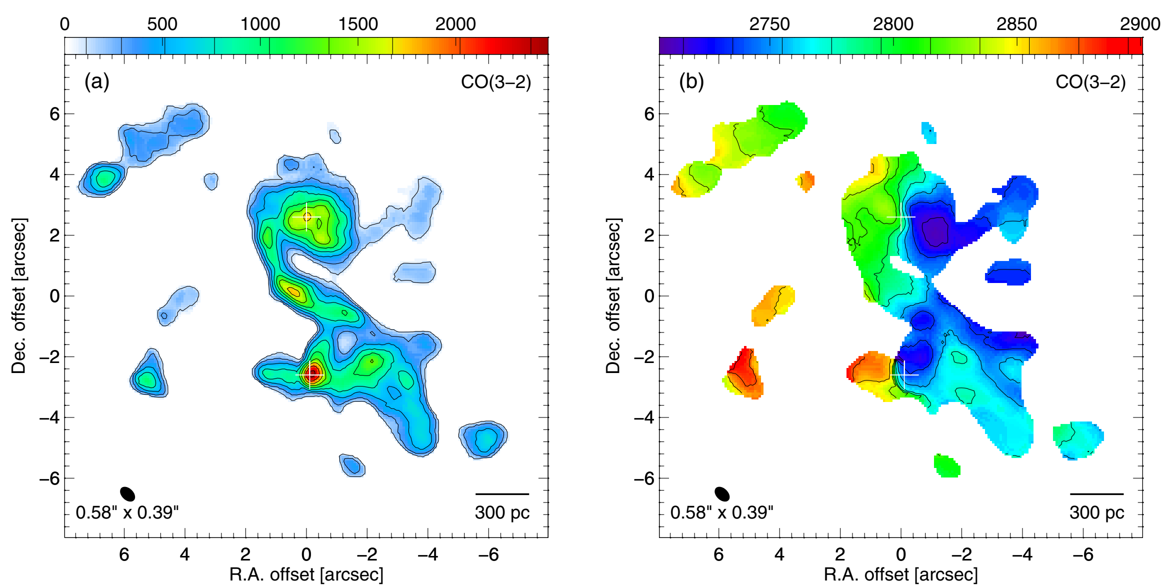

Figure 7. CO(3–2) moment 0 and 1 maps (i.e., integrated intensity and mean velocity maps) made with a high cutoff for the moment analysis to emphasize the brightest circumnuclear emission. The intensity map (a) is corrected for the mosaic sensitivity patterns. The nth contours are at $110n^{1.4}$ K km s^{-1}. The velocity contours in Panel (b) are at 2775 km s^{-1} and every 20 km s^{-1} from it. The two white plus signs are at the positions of the cm-wave nuclei.

(A color version of this figure is available in the online journal.)

have lower excitation temperatures than ^{12}CO (i.e., subthermally excited), or are emitted from smaller regions than the ^{12}CO lines.

3.2.4. Line Flux, Gas Mass, and Surface Density

The total CO flux is measured to be 1.0×10^3, 3.0×10^3, and 5.7×10^3 Jy km s^{-1} for the $J = 1$–0, 2–1, and 3–2 transitions, respectively, in a 20″ diameter aperture centered at the midpoint of the two nuclei. The CO(1–0) flux in the concentric 40″ diameter aperture is 1.6×10^3 Jy km s^{-1}. These are corrected for the primary beam (and mosaic) responses, but not for any missing flux in the interferometric data. These fluxes are measured in data cubes with resolutions ∼2.″7, ∼0.″6, and ∼0.″6

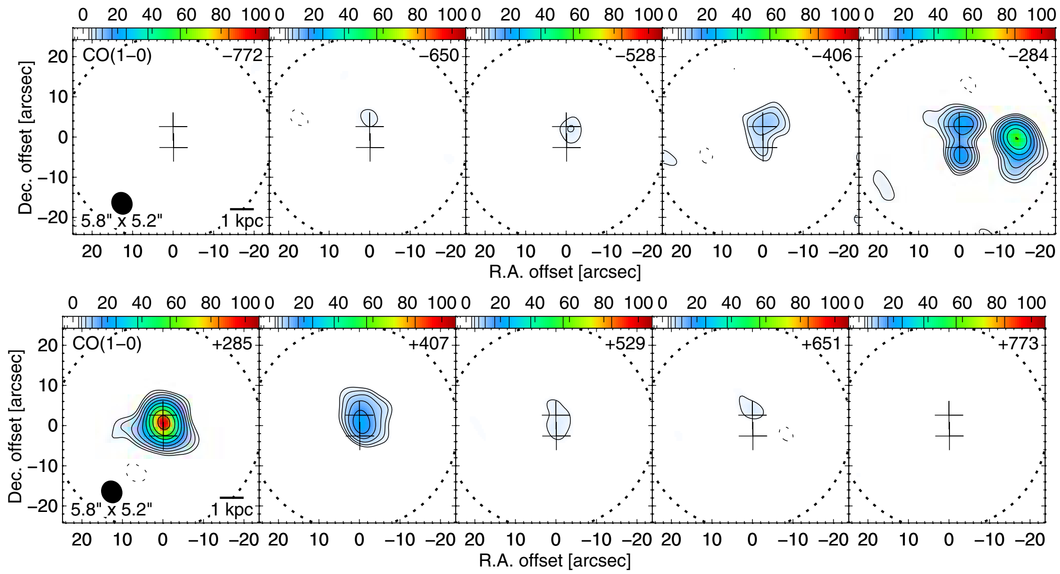

Figure 8. CO(1–0) channel maps made for high-velocity emission with uv tapering. Each channel is 122 km s^{-1} wide. Velocity offsets from 2775 km s^{-1} are at the top-right corners. Contours are at $\pm 3 \times 1.5^n \sigma$ ($n = 0, 1, 2, 3, \cdots$), where the rms noise is $\sigma = 1.1$ mK. Negative contours are dashed. The data are not corrected for the mosaicked primary-beam response, whose 50% contours are the dotted circles. The peak intensity of CO(1–0) in these channels is 101 mK while that of the 2.6 mm continuum already subtracted here is 30 mK at this resolution. The intensity scale bars at the top are labeled in mK. The two plus signs in each panel are at the two nuclei. The black ellipse in the bottom-left corner of each leftmost panel shows the FWHM size of the observing beam.

(A color version of this figure is available in the online journal.)

for CO(1–0), (2–1), and (3–2), respectively. The CO(2–1) flux in the same 20″ aperture is 4.0×10^3 Jy km s^{-1} in a ∼3.″0 resolution data cube.

The CO(2–1) to CO(1–0) flux ratio at about 3″ resolution is 4.0 with ∼10% calibration uncertainty. This is expected for the thermalized optically thick gas at ≳30 K. The two data sets have about the same range of baseline length in units of wavelength, so the ratio is not significantly affected by missing flux. The CO(3–2) to (2–1) ratio at about 0.″6 resolution is 1.9 in flux and 0.86 in brightness temperature. This is fully compatible with thermalized optically thick CO at ≳30 K, considering the calibration uncertainties and the expected missing flux in the CO(3–2) data. On the whole, the data are consistent with the CO being thermalized at least up to $J = 3$ and optically thick.

We estimate the mass of molecular gas using the CO(1–0) to H_2 conversion factor $X_{CO} \equiv N_{H_2}/I_{CO(1-0)} = 1 \times 10^{20}$ cm^{-2} (K km s^{-1})$^{-1}$ and 36% mass contribution from He. We do not have the true X_{CO} in NGC 3256 nor do we have a strong reason to believe that X_{CO} is constant across the galaxy. Therefore, we give our molecular gas masses with the parameter X_{20} that is X_{CO} in units of 1×10^{20} cm^{-2} (K km s^{-1})$^{-1}$. While X_{20} is unity for our assumed (i.e., fiducial) conversion factor, this parameterization allows our mass estimates to be easily rescaled when a more plausible value of X_{CO} is found. The conversion factors estimated with various methods in galaxies at solar metallicities or higher are usually in the range of $X_{20} = 0.3$– 3, with high values for "normal" galaxies (such as our Galaxy in its disk) and low values for luminous infrared galaxies (see Bryant & Scoville 1996, Downes & Solomon 1998, and a recent review by Bolatto et al. 2013b). Bolatto et al. (2013b) recommend $X_{20} = 0.4$ with an uncertainty of 0.5 dex for luminous starburst galaxies and SHP06 obtained a value within 10% of this for the central 3 kpc of NGC 3256 after averaging various estimates. In this paper, however, we adopt the normalization with $X_{20} = 1$ partly for simplicity, and also because the gas-to-dynamical mass ratios that we later calculate for the nuclei, and for a larger area, appear more reasonable with $X_{20} = 1$. In any case, we expect a factor of three uncertainty in our adopted X_{20} of 1.0, so 0.4 is within the uncertainty. The conversion factor between CO(1–0) integrated intensity and molecular gas surface density is $\alpha_{CO} \equiv \Sigma_{mol}/I_{CO(1-0)} = 2.2 X_{20}\, M_\odot$ pc^{-2} (K km s^{-1})$^{-1}$.

The molecular gas mass estimated from our CO(1–0) data is M_{mol} ($r \leqslant 10''$) $= 7 \times 10^9 X_{20}\, M_\odot$ in the central 20″diameter aperture and M_{mol} ($r \leqslant 20''$) $= 1 \times 10^{10} X_{20}\, M_\odot$ for the central 40″ (7 kpc). The scaling parameter X_{20} should be read as the average value for each region in consideration. The peak molecular gas surface densities toward individual nuclei at 1.″4 (240 pc) resolution are calculated to be $4 \times 10^3 X_{20}$ and $3 \times 10^3 X_{20}\, M_\odot$ pc^{-2}% for the northern and southern nuclei, respectively, from the CO(1–0) data in Figure 2. The southern nucleus has the highest CO integrated intensity in the merger, with a peak gas column density of $\Sigma_{mol}(S) = 6 \times 10^3 X_{20}\, M_\odot$ pc^{-2}% in our ∼0.″5 (80 pc) resolution CO(3–2) data in Figure 2. Here we do not correct for the different transition because of the CO excitation inferred above. Converting this to the peak hydrogen and proton column densities, we obtain $\log(N_{H,equiv.}/\mathrm{cm}^{-2}) = 23.9$ and $\log(N_p/\mathrm{cm}^{-2}) = 23.8$ toward the southern nucleus. The former converts H_2 and He with hydrogen atoms of equivalent mass and the latter gives proton column density. Both have 0.5 dex uncertainty inherited from the uncertainty in X_{20}.

3.3. *High-velocity Emission*

We detected wide, faint line wings in our data, most clearly in CO(1–0) and (3–2), and also in CN(1–0). The new sensitive ALMA data not only confirm the previous detection of SHP06, but also better constrain the velocity extent and spatial distribution of the high-velocity gas.

3.3.1. *Channel Maps*

Figures 8 and 9 show our CO(1–0) and CN(1–0) channel maps, respectively, made with u–v tapering (i.e., spatial

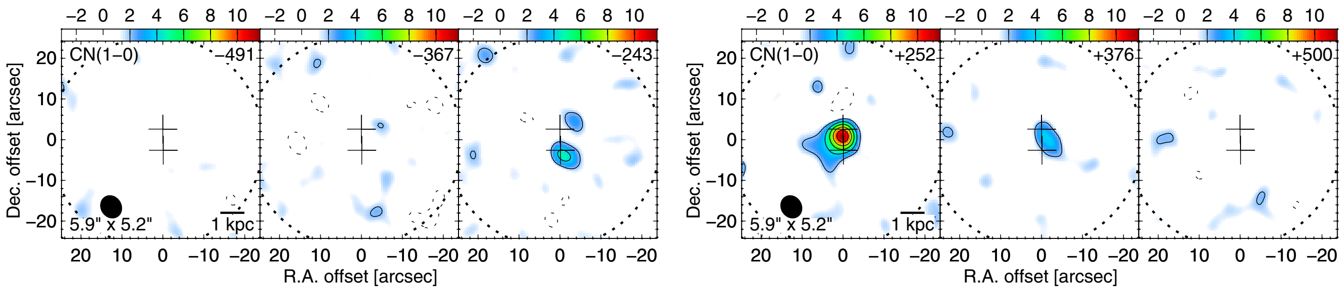

Figure 9. CN(1–0, 3/2–1/2) channel maps made for high-velocity emission with uv tapering. Each channel is 124 km s^{-1} wide. Velocity offsets from 2775 km s^{-1} are at the top-right corners. Contours are at $\pm 2.5n\sigma$ ($n = 1, 2, 3, \cdots$), where the rms noise is $\sigma = 0.80$ mK. Negative contours are dashed. The data are not corrected for the mosaicked primary-beam response, whose 50% contours are the dotted circles. The peak intensity of the CN(1–0) line in these channels is 11.7 mK. The intensity scale bars at the top are labeled in mK. The two plus signs in each panel are at the two nuclei. The black ellipses in the bottom-left corners show the FWHM size of the synthesized beam.

(A color version of this figure is available in the online journal.)

smoothing) and wide channel widths to better detect high-velocity emission. These Band 3 images use the combined CSV and Cycle 0 data to maximize sensitivity. Continuum was determined more than 750 (400) km s^{-1} away from $V_{\rm sys}$ for the CO (CN) lines and has already been subtracted. The CO(1–0) data show $>3\sigma$ emission from -650 km s^{-1} to $+650$ km s^{-1} around the northern nucleus, up to about 500 km s^{-1} from $V_{\rm sys}$ between the two nuclei, and up to $\sim V_{\rm sys} \pm 400$ km s^{-1} around the southern nucleus. At about $V_{\rm sys} \pm 300$ km s^{-1}, the redshifted emission is stronger than the blueshifted emission and peaks between the two nuclei. The same is observed in CN(1–0), and was also the case in the CO(2–1) observations of SHP06 in which the wing emission was first found up to $V_{\rm sys} \pm 300$ km s^{-1}.

Figure 10 shows CO(3–2) channel maps displaying blueshifted and redshifted emission on the same panel for the same absolute offset from $V_{\rm sys}$. The background image in gray is continuum. The upper panels (Figure 10(a)) are our 1″.1 resolution data. Emission stronger than 4σ is detected up to $V_{\rm sys} \pm 450$ km s^{-1}. The northern nucleus has emission up to this largest offset velocity and the centroid of the blueshifted emission is on the northwestern side of the nucleus, while the redshifted emission centroid is on the southeastern side. Around the southern nucleus, redshifted and blueshifted emission are roughly symmetrical about the nucleus, redshifted to the north and blueshifted to the south, except the redshifted emission extends east from the southern nucleus at the leftmost channel. Also notable is that emission more than about 300 km s^{-1} from $V_{\rm sys}$ is clearly detached from the southern nucleus, unlike the high-velocity emission around the northern nucleus. The lower panels (Figure 10(b)) are from our 0″.5 resolution data. The symmetry around the southern nucleus is evident. The new observations here are: the high-velocity gas has clumps in the extended structures and the blueshifted gas slightly curves toward the west at larger distances from the southern nucleus. Again, the highest velocity emission is clearly separated from the southern nucleus by about 1″.8 (310 pc). Little line emission is detected around the northern nucleus in these higher resolution data. This indicates that the high-velocity CO(3–2) emission is more extended around the northern nucleus than around the southern nucleus. The same is seen in the high-velocity blueshifted CO(1–0) in Figure 11(a).

3.3.2. *High-velocity Line Flux*

The flux of the high-velocity CO emission has been measured in two 530 km s^{-1} wide ranges offset by about 220–750 km s^{-1} from 2775 km s^{-1} ($V_{\rm sys}$). Figure 11 shows CO(1–0) maps for these velocities. The CO(1–0) flux in our 2″.7 resolution data (Figure 11(b)) is 8.9, 3.2, and 1.2 Jy km s^{-1} for the redshifted emission, blueshifted emission associated with the northern nucleus, and blueshifted emission associated with the southern nucleus, respectively. The response of the primary beam was corrected for these measurements. We excluded the blueshifted emission about 15″ east of the nuclei because it is associated with an arm there and is detected only down to about $V_{\rm sys} - 300$ km s^{-1}. In total, this high-velocity emission has 1.3% of the total CO(1–0) flux in the central 20″ diameter aperture (Section 3.2.4). In our 0″.6 resolution data, the CO(3–2) flux in the same velocity ranges are 40, 11, and 21 Jy km s^{-1} for the redshifted emission, blueshifted emission associated with the northern nucleus, and blueshifted emission associated with the southern nucleus, respectively. In total, this high-velocity emission has 1.2% of the total CO(3–2) flux in the central 20″ given in Section 3.2.4.

3.3.3. *High-velocity Gas Mass*

The total mass of the high-velocity molecular gas is calculated to be $M_{\rm mol}$ (223 km s^{-1} $\leqslant |V - V_{\rm sys}| \leqslant$ 752 km s^{-1}) $=$ $8.8 \times 10^7 X_{20}\, M_\odot$ from the high-velocity CO(1–0) line flux. The mass of high-velocity molecular gas associated with each nucleus is estimated to be $6.3 \times 10^7 X_{20}\, M_\odot$ for the northern nucleus and $2.5 \times 10^7 X_{20}\, M_\odot$ for the southern nucleus under the assumption that the redshifted high-velocity gas is composed of gas associated with the two nuclei, with the same fractions as in the blueshifted high-velocity gas (i.e., 72% to the north and 28% to the south). We use the ratio in our CO(1–0) data and not the ratio of N:S = 34:66 in our CO(3–2) data because the former data suffer less from missing flux. Also CO(1–0) is less affected by any difficulty in CO excitation in the high-velocity gas.

We assume, unless otherwise noted, that X_{20} is unity for the high-velocity gas, as we did for the bulk CO emission of NGC 3256. This is partly motivated by our observation that the fraction of the high-velocity flux to the total flux is almost the same in CO(1–0) and CO(3–2). This may be because the physical properties are not drastically different between the high-velocity gas and the gas at lower velocities.

A possible alternative choice of $X_{\rm CO}$ for the high-velocity gas is the one for optically thin CO emission. This is possible because the high-velocity emission's peak CO brightness temperature is only on the order of 0.5 K for CO(1–0) and 1.5 K for CO(3–2) in Figures 4 and 5. In beam-matched data of 1″.6 × 1″.2 resolution, the CO(3–2) to CO(1–0) ratios of peak brightness

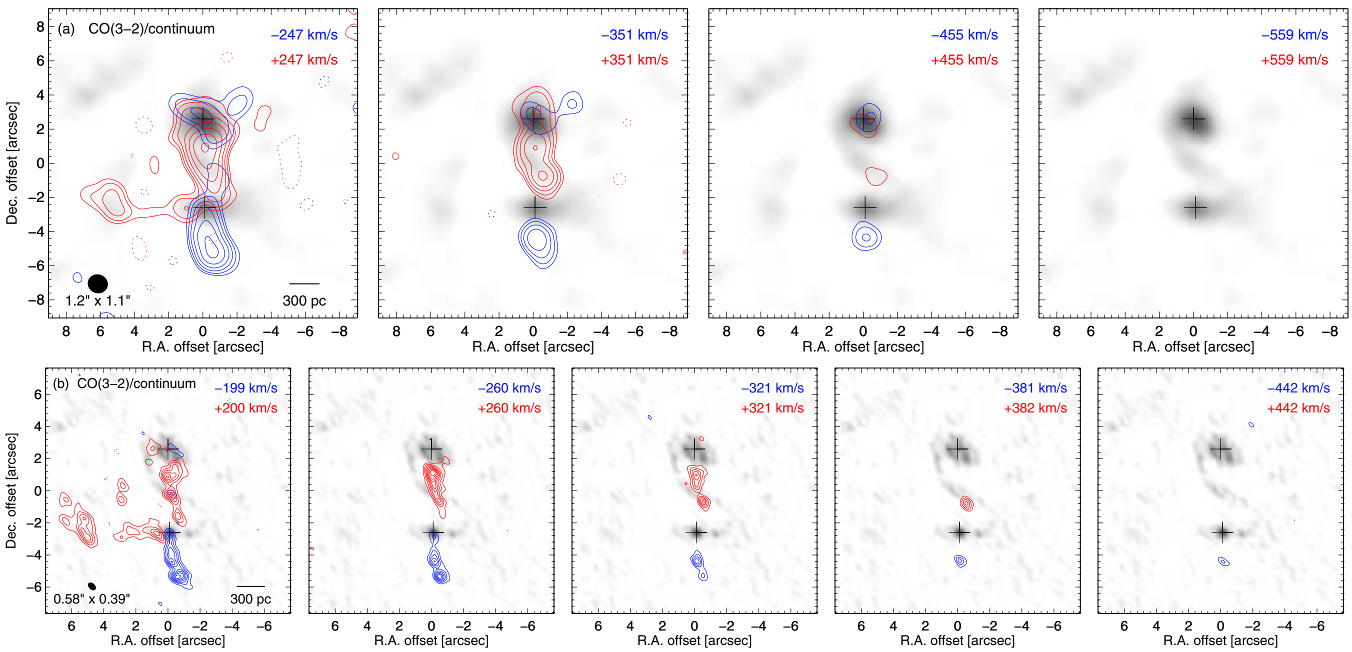

Figure 10. CO(3–2) channel maps of high-velocity emission at 1″.1 (a; upper row) and 0″.5 (b; lower row) resolutions. Red and blue contours (gray and black in the printed journal) in each panel are respectively for a channel redshifted or blueshifted by the amount indicated in the top-right corner from the fiducial velocity 2775 km s^{-1}. In (a) [(b)], each channel is 104 [61] km s^{-1} wide and contours are at $\pm 4 \times 1.8^n \sigma$ ($n = 0, 1, 2, 3, \cdots$) [$\pm 4n\sigma$ ($n = 1, 2, 3, \cdots$)], where the rms noise is $\sigma = 5.6$ [38] mK. Negative contours are dashed. The background grayscale image is 0.86 mm continuum emission at the same resolution. The peak continuum intensity is 108 [237] mK. These data are not corrected for the mosaicked primary-beam response, whose FWHM size is about 24″. The two plus signs in each panel show the locations of the two radio nuclei. The leftmost panel in each row has a scale bar and an ellipse showing the FWHM size of the observing beam.

(A color version of this figure is available in the online journal.)

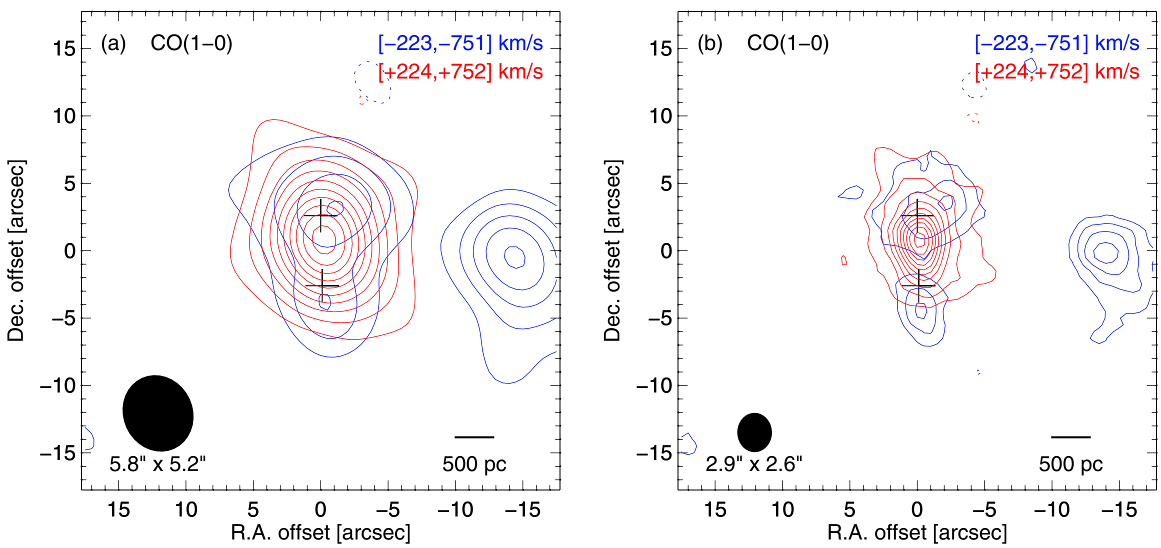

Figure 11. CO(1–0) maps of high-velocity emission at different spatial resolutions. Red and blue contours (gray and black in the printed journal) are intensities integrated over 528 km s^{-1} at, respectively, redshifted and blueshifted velocity ranges indicated in the top-right corner. They are offsets from the fiducial velocity 2775 km s^{-1}. Contours are at $\pm 4n^p\sigma$ ($n = 1, 2, 3, \cdots$) where $p = 1.2$ and $\sigma = 0.24$ K km s^{-1} in Panel (a) and $p = 1.1$, $\sigma = 0.79$ K km s^{-1} in Panel (b). Negative contours are dashed. The data are not corrected for the primary-beam response whose FWHM size is 53″. The two plus signs are at the two nuclei. The ellipse at the bottom-left corner shows the FWHM size of the synthesized beam.

(A color version of this figure is available in the online journal.)

temperatures around $V_{\rm sys} \pm 200$ km s^{-1} are mostly $\sim 1 \pm 0.5$ for the high-velocity emission associated with the southern nucleus. Taken at face value, assuming little effect of CO(3–2) missing flux to this ratio because the high-velocity gas around the southern nucleus is relatively compact, the ratio may be due not only to optically thick emission from thermalized CO but also to optically thin CO emission. In the latter case, the ratio corresponds to the excitation temperature of 12 ± 3 K in LTE. If the CO excitation is non-LTE then CO(1–0) can have a higher excitation temperature than this LTE temperature, but the CO(3–2) excitation temperature must be much lower than 12 K. The conversion factor for optically thin CO(1–0) emission is on the order of $X_{20} = 0.1$ in both the LTE and non-LTE cases for a CO abundance of $[{\rm CO/H_2}] = 10^{-4}$. The non-LTE

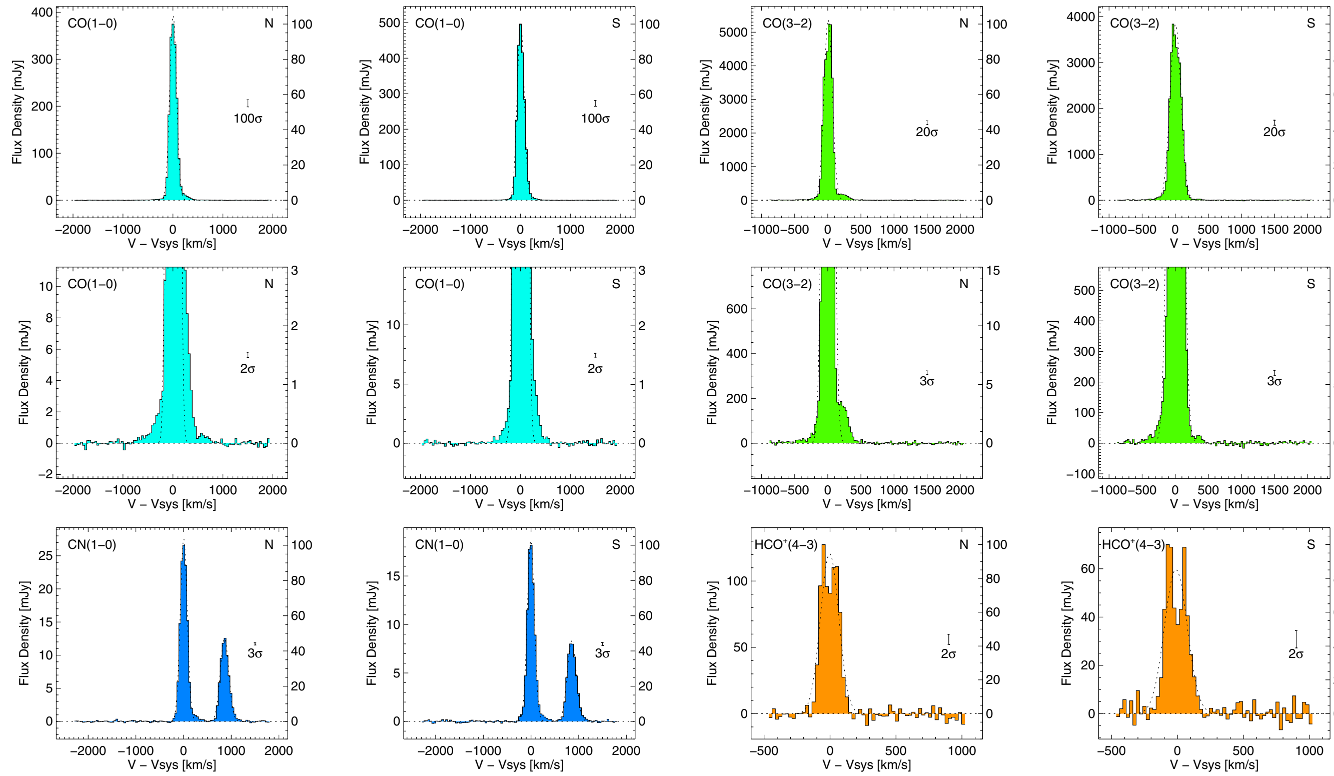

Figure 12. Line spectra at the NGC 3256 nuclei. Line names are in individual panels. The left column in each pair is for the northern nucleus and the right for the southern nucleus. Dotted curves are single-component Gaussian fits to the data to help identify excess emission at high velocities. Abscissa is velocity offset from $2775\,\mathrm{km\,s^{-1}}$. Right ordinate is fraction in percent of the peak in the spectrum. (Row 1) CO(1–0) spectra are sampled with 4″ diameter apertures from the CSV + Cycle 0 data of ∼5″ resolution. CO(3–2) spectra are sampled with 4″ diameter apertures from a data cube having spatial and spectral resolutions of ∼0.″6 and $26\,\mathrm{km\,s^{-1}}$, respectively. (Row 2) Same as Row 1 except that only the small ranges of ordinate near zero are shown for line wings. (Row 3) CN(1–0) spectra are sampled with 4″ diameter apertures from the CSV + Cycle 0 data of ∼5″ resolution. The abscissa is for the brighter CN(1–0, 3/2–1/2) line and two-component Gaussian fit is made for the two transitions. HCO^+(4–3) spectra are sampled with 2″ diameter apertures from ∼0.″6 resolution data.

(A color version of this figure is available in the online journal.)

conversion factor for optically thin CO(1–0) depends little on gas temperatures above ∼15 K, provided that CO molecules are well excited only to $J = 2$ but not to 3 and beyond. The CO level population is determined by the level statistical weights in such a case. As the observed line ratio is consistent with varied gas conditions, keep in mind that X_{20} for the high-velocity gas may be an order of magnitude lower than our fiducial value of unity.

3.3.4. Spectra

Figure 12 shows spectra measured at the two nuclei. Each line is fitted with a Gaussian to highlight the high-velocity wings (i.e., emission in excess of the Gaussian fit at large offset velocities). At both nuclei, line centroids are within about $10\,\mathrm{km\,s^{-1}}$ from our fiducial velocity of $2775\,\mathrm{km\,s^{-1}}$ and line FWHM are about 150–200 $\mathrm{km\,s^{-1}}$.

The CO(1–0) data have the highest signal-to-noise ratio (S/N) and show a clear redshifted wing toward the northern nucleus at the level of ∼3% of the peak. There are also high-velocity wings at the level of 1% or less in both redshifted and blueshifted velocities. The full width at zero intensity (FWZI) of the emission is about $1800\,\mathrm{km\,s^{-1}}$ toward the northern nucleus; this is the width between the first nulls of the line profile. The southern nucleus also has blueshifted and redshifted wings at the 1%–2% level of the main line, again with the red wing stronger. The fraction of the wing component to the main line is probably larger when the wing features are extrapolated from both sides to the systemic velocity. The FWZI for the southern nucleus is about $1300\,\mathrm{km\,s^{-1}}$. These parameters are consistent with Figure 8, where the full line widths are $\gtrsim 1000\,\mathrm{km\,s^{-1}}$, the line is wider toward the northern nucleus, and the high-velocity emission is stronger in redshifted velocities at around $|V - V_{\mathrm{sys}}| = 300\,\mathrm{km\,s^{-1}}$.

The CO(3–2) spectra also show the high-velocity wings. More emission is in the redshifted wing, in the aperture containing the northern nucleus. Fainter and broader wings are seen in both bluehifted and redshifted velocities toward both nuclei. The full width of the CO(3–2) line is about $1000\,\mathrm{km\,s^{-1}}$ in our data, consistent with that in channel maps (Figure 10(a)). The narrower profile in CO(3–2) versus in CO(1–0) must be partly due to the lower S/N in the former data.

In HCO^+(4–3) we did not detect high-velocity emission. This may be mostly because HCO^+(4–3) has the lowest S/N among the lines shown in Figure 12 and also because the $J = 4$ excitation of HCO^+ has a high critical density of $10^7\,\mathrm{cm^{-3}}$. The HCO^+ line profiles have double peaks (or a dip near the line center) toward both nuclei. This is also seen in CO(3–2) toward the southern nucleus with a smaller 2″ diameter aperture.

3.3.5. CN in the High-velocity Gas

The CN(1–0) spectra in Figure 12 show the redshifted wing at about the same level as in the CO(1–0) data. Although each of the CN lines consists of a group of hyperfine lines, the redshifted wing is not due to the line distribution because if it were then the redshifted emission in Figure 9 should have peaked on the nuclei and not between them. Thus both CN and CO red wings are probably from the same high-velocity gas. The flux ratio of

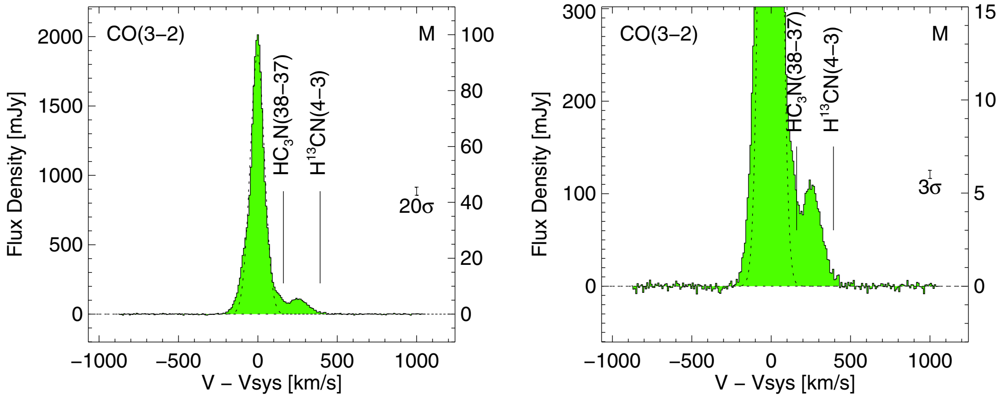

Figure 13. CO(3–2) spectrum sampled with a 2″ diameter aperture at the midpoint of the two nuclei from a cube of 1″.15 and 8.7 km s^{-1} resolutions. The same spectrum is plotted twice with different y axis ranges. HC$_3$N(38–37) and H^{13}CN(4–3) lines should appear at the marked locations if emitted from gas at the velocity of the CO(3–2) line peak.

(A color version of this figure is available in the online journal.)

the two CN lines is 1.8 toward both nuclei, only slightly less than the ratio of 2 from optically thin lines (Turner & Gammon 1975). The CN emission is, therefore, mostly optically thin; the opacity of the brighter line is calculated to be 0.4 from $(1 - e^{-\tau})/(1 - e^{-\tau/2}) = 1.8$. Using the safe assumption that the low-velocity CO(1–0) with peak $T_b \gtrsim 10$ K is optically thick and has a higher optical depth than the high-velocity CO emission, the fraction of the high-velocity emission to the main low-velocity component should be larger in CN than in CO after the CO opacity correction. This suggests enhanced CN abundance or excitation in the high-velocity gas. If the CN enhancement is due solely to collisional excitation, then the high-velocity gas is denser than the low-velocity gas. This is because the critical density for CN(1–0) is 10^6 cm^{-3} and is 10^3 times higher than that for CO(1–0). This CN detection in the high-velocity gas, as well as its enhancement there, is particularly noteworthy because the line has not been detected in galactic molecular outflows before.

3.3.6. Robustness of the Detection

Our detection of the high-velocity emission is robust for the following reasons. First, continuum subtraction errors cannot explain these line wings. This is because much of the high-velocity emission is offset from the continuum nuclei where the largest artifacts are expected, and also because the wing emission is too strong to be due to passband calibration error. The continuum in each channel is only at the levels of 30σ and 20σ in our CO(1–0) and (3–2) data, respectively. The flatness of our spectra sufficiently away from the line (Figure 12) indicates that our passband calibration is much more accurate than 1/30 or 3%. Second, the high-velocity emission is unlikely to be due to line blending, i.e., lines other than the target line. This is due to the offset of the high-velocity emission from the nuclei where all lines peak, and also because of the lack of molecules that may plausibly contribute to the wing emission. Individual line wings in our data sometimes have possible alternative identifications, such as HC$_3$N(38–37) and H^{13}CN(4–3) for the red (i.e., low-frequency) wing of CO(3–2). However, these molecules do not have transitions adjacent to CO(2–1) or CO(1–0) and hence cannot explain their line wings. In addition, Figure 13 indicates that the red wing of CO(3–2) cannot be due to HC$_3$N(38–37) and H^{13}CN(4–3) as long as their profiles are similar to the CO line profile. Finally, the line wings are not likely due to the response pattern of the spectral correlator to a strong narrow line, as this would appear symmetric about the line center.

3.3.7. Position–Velocity Diagrams

Figure 14 shows CO position–velocity (PV) diagrams across the nuclei. The inset in each panel indicates the location and position angle of the cut. The p.a. = 270° for the northern nucleus is along the kinematic major axis at the center of the northern circumnuclear disk. The p.a. = 270° for the southern nucleus is because there is a structure extending across the nucleus in this direction. The PV diagrams along p.a. = 0° contain both nuclei and the high-velocity emission that appears symmetric about the southern nucleus along this axis. Rotation of the northern circumnuclear disk is evident in Panels (a) and (d), as is the high-velocity emission at the northern nucleus. Gas motion around the southern nucleus is more complex, in particular in the CO(3–2) data in Panel (e). But an overall velocity gradient within ∼5″ from the nucleus, and the presence of high-velocity gas at the nucleus, are consistent with those in the channel maps.

Most interestingly, we clearly see two components of high-velocity gas in the PV diagrams (c) and (f). One is on the northern nucleus and shows little positional shift with velocity. The other is symmetric about the southern nucleus, and blueshifted to the south (left) and redshifted to the north within about 4″ from the nucleus. The terminal velocity increases with distance from the southern nucleus, up to about the offset of 2″. It is also notable that the range of emission velocities at each position is as large as ∼500 km s^{-1} across this region of a north–south velocity gradient.

3.4. Comparison with Other Observations

3.4.1. HST Optical Images

Figure 15 compares our CO maps with multi-color *Hubble Space Telescope* (*HST*) images of NGC 3256. The merger has many dark lanes, particularly in the southern part, as seen in Panels (a) and (c). Comparison of the optical image in Panel (a) with the color excess image in Panel (b) shows that the dark lanes are generally redder in color than their adjacent areas, suggesting that these dark lanes are due to higher dust extinction. Panels (a) and (c) show an overall match between the dark lanes in the optical and the CO distribution in contours; Panel (d) helps to read CO(3–2) intensities. This is expected when these dark lanes are due to obscuration by the interstellar dust. In addition, there is an interesting match between the dark lanes (i.e., optical color excess) and the CO line widths as shown in Panel (b).

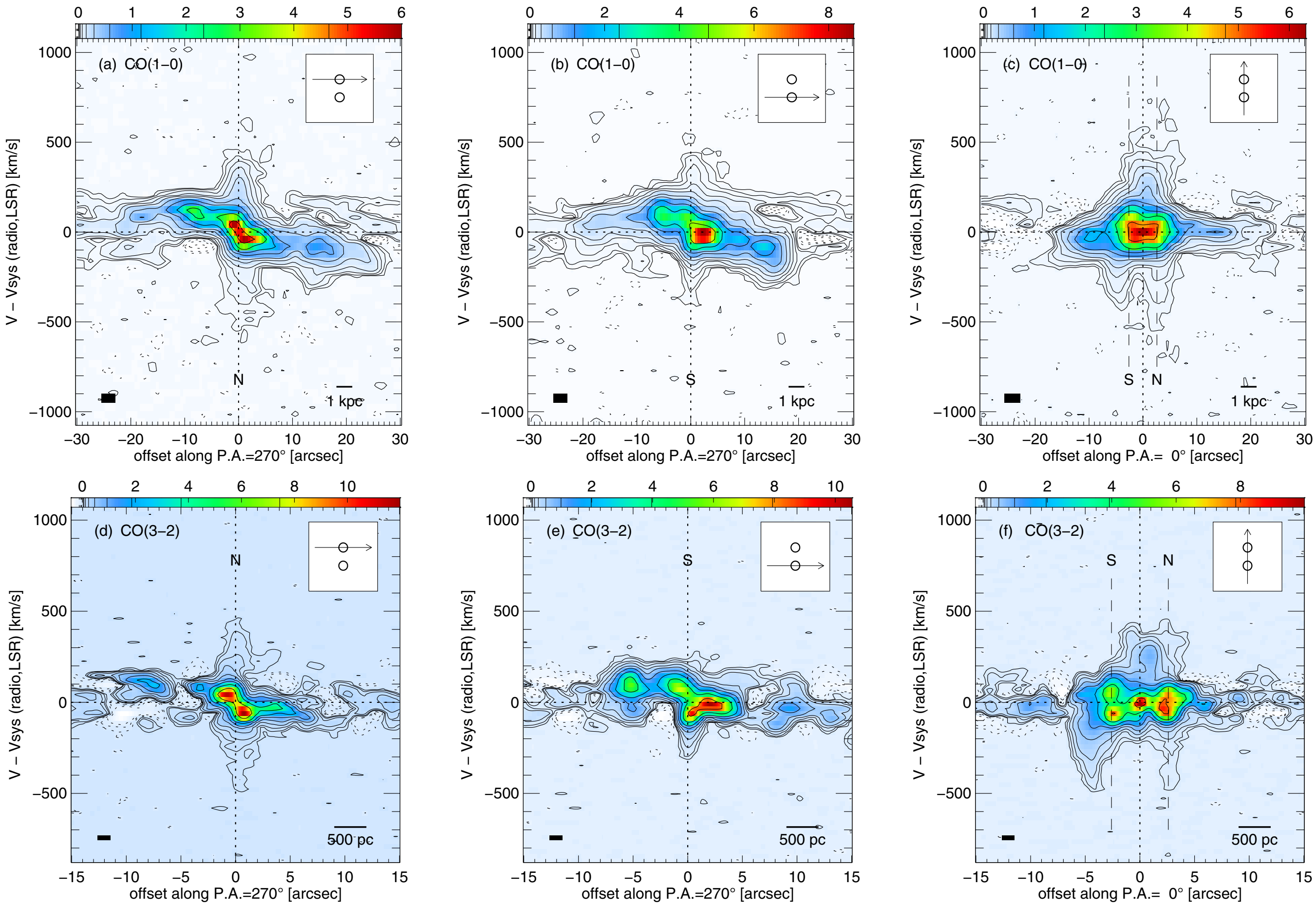

Figure 14. CO position–velocity cuts through the nuclei. The upper row is for CO(1–0) and lower CO(3–2). The three columns are (left) p.a. = 270° cut through the N nucleus, (middle) p.a. = 270° cut through the S nucleus, (right) p.a. = 0° cut through the midpoint of the N and S nuclei. The locations of the two nuclei are marked with the letters N and S. The inset in each panel illustrates the cut with respect to the two nuclei. For CO(1–0), each cut is 2$''$.5 wide and the data resolution is ~2$''$.7. Contours are at $\pm 2 \times 2^n \sigma$ ($n = 0, 1, 2, 3, \ldots$), where $\sigma = 4.6$ mK. For CO(3–2), the slit width and the data spatial resolution are both 1$''$.1. Contours are at $\pm 2.5 \times 2^n \sigma$ ($n = 0, 1, 2, 3, \ldots$), where $\sigma = 12$ mK. Negative contours are dashed. The intensity scale bars are labeled in kelvin. The resolution element is shown as a black rectangle in the bottom-left corner.

(A color version of this figure is available in the online journal.)

Both are enhanced in a roughly triangular area on the south-western side of the binary nucleus, although the coincidence is poor in the vicinity of the two nuclei (see also Figure 2 for our CO(3–2) second moment map).

3.4.2. VLA Radio Continuum Images

There are remarkable correlations between our ALMA data and VLA radio continuum data in Neff et al. (2003). The spatial distribution of 6 and 3.6 cm continuum in their Figure 1 matches quite well with that of the sub/millimeter continuum shown in our Figure 1. Our Figure 16(a) shows their 3.6 cm data for comparison. The agreement includes the two nuclei and the overall shape of the diffuse emission, a short arc (arm) about 5$''$ northeast of the northern nucleus, a spot about 20$''$ west of the same nucleus, the bridge-like arm emanating from the northern nuclear disk to the south, and a linear feature crossing the southern nucleus in the east-west direction. The 3.6 cm image also shows a radio spur, marked with an arrow in Figure 16(a), arising from the southern nucleus to the south and slightly curving toward the west. It has a counterpart in our CO data: The blueshifted emission in the $|V - V_{\rm sys}| = 200$ km s^{-1} channel of Figure 10(b) coincides with the radio spur. Since this radio spur is much more elongated than the VLA beam, and curves in the same way as the CO feature, we judge it to be a real feature rather than a sidelobe.

Figure 16(b) compares a higher resolution 3.6 cm image from Figure 2 of Neff et al. (2003) with our ALMA data. The 3.6 cm continuum in black contours and 860 μm continuum in gray scale again show very good correlation. In the radio data there is a pair of narrow spurs that emanate from the southern nucleus to the north and south. The one to the south coincides with a part of the curved radio spur mentioned previously and marked in Figure 16(a). This strengthens the presence of the radio feature. Although we did not detect these spurs in submillimeter continuum, our CO data show their counterparts. The highest velocity CO(3–2) emission shown in red and blue contours are at the tips of these radio spurs. We discuss these observations in Section 5.2.6.

3.4.3. Spitzer Infrared Images

Figure 17 shows an archival 5.8 μm image and a color composite made from 8, 5.8, and 4.5 μm images taken with the *Spitzer Space Telescope* Infrared Array Camera (Program ID 32). The 2$''$ resolution images show the same area as in Figure 1(a), our 2.8 mm continuum image, and the 5.8 μm image uses the same linear intensity scale as in Figure 1(a).

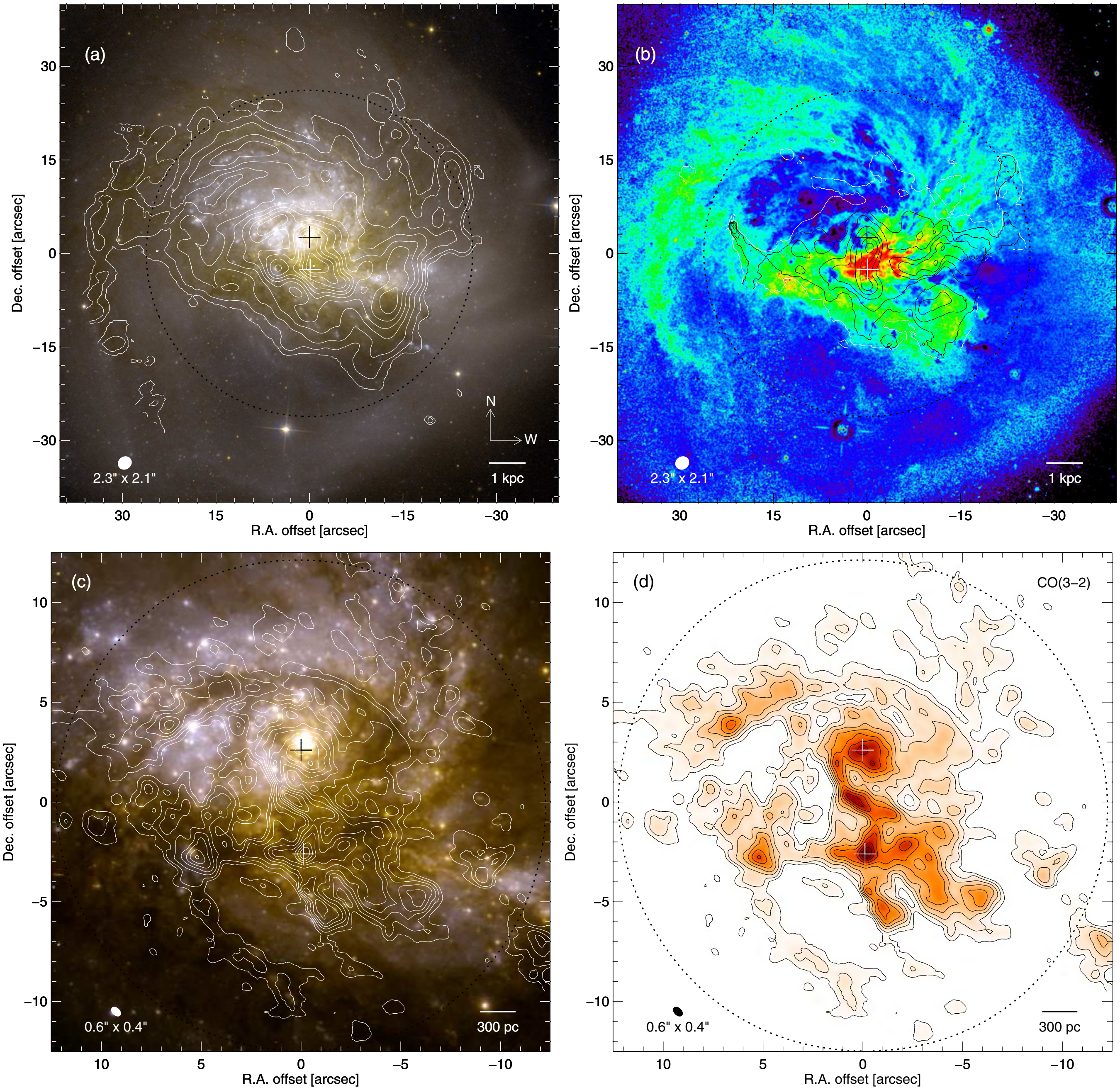

Figure 15. Comparison of *HST* and ALMA CO data. (a) A composite of F814W ($\sim I$) and F435W ($\sim B$). Contours are CO(1–0) emission with the nth contours at $0.2n^{2.5}$% of the peak integrated intensity 1340 K km s^{-1}. (b) $B-I$ color index with overlaid contours of CO(1–0) line width (i.e., 2nd moment). Contours are in 10 km s^{-1} steps starting from 20 km s^{-1} and in white at the lowest level and black above. Much of CO(1–0) emission has corresponding optical dark lanes. Regions with red optical colors generally have larger CO line widths. (c) CO(3–2) contours on the *HST B* and *I* composite image. The nth contours are at n^2% of the peak integrated intensity 2730 K km s^{-1}. There may be a small ($\sim 0\farcs5$) astrometric offset between the radio and optical data. (d) CO(3–2) velocity-integrated intensity with the same contours as in Panel (c). In each panel, the two plus signs are at the radio nuclei and the dotted circle is the 50% contour of the ALMA primary beam response, for which the CO data are corrected.

Similarities exist between the infrared and millimeter continuum distributions both in the two bright nuclei and the extended features around them. These similarities include the spiral arm to the north of the nuclei, bright areas about 5″ and 20″ east of the northern nucleus, and a linear feature that protrudes west from the central region by about 15″ at about the latitude of the southern nucleus. The northern nucleus is brighter than the southern nucleus, except at 4.5 μm (hence the blue color of the latter in the color composite), and even more so at 11.5 μm (Lira et al. 2008). We saw this in 860 μm continuum (Section 3.1 and Table 7). The 8–1000 μm luminosities of the northern and southern nuclei in $\sim 3''$ diameter apertures have been estimated to be $2.9 \times 10^{10}\ L_\odot$ and $1.5 \times 10^{10}\ L_\odot$, respectively, from SED template fitting to the infrared data (Ohyama et al. 2014).

4. MERGER CONFIGURATION

We adopt the merger configuration in Figure 18 on the basis of previous studies and our observations. The figure shows two

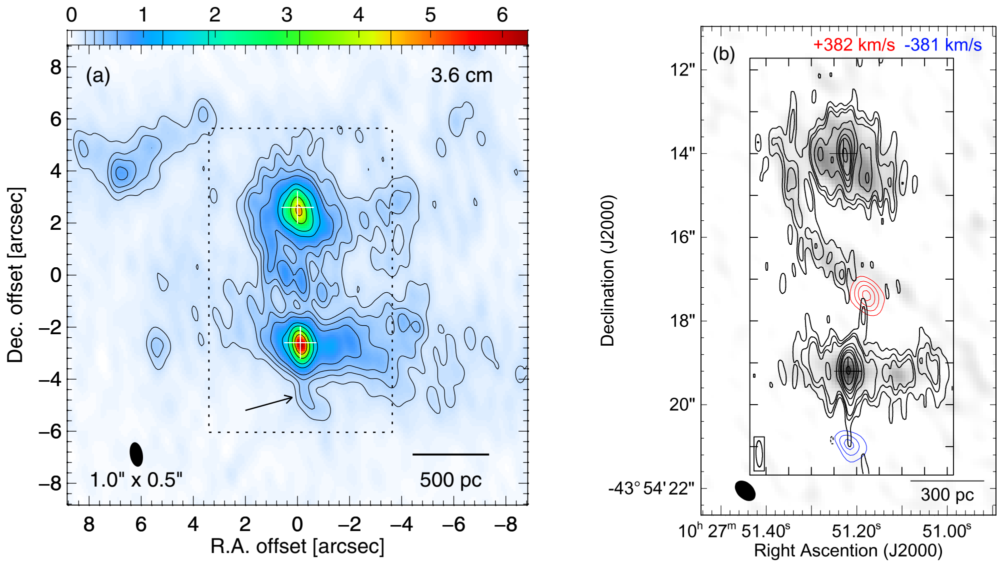

Figure 16. (a) VLA 3.6 cm continuum image from Neff et al. (2003). Contours are at 0.19, 0.32, 0.44, 0.64, 1.3, 1.9, 3.2, and 4.4 mJy beam^{-1} (rms $\sim$ 21 μJy beam^{-1}). The dotted rectangle is the outer frame of the Panel (b). An arrow points to the radio spur mentioned in the text. (b) Comparison of 3.6 cm continuum (black contours) with 0.86 mm continuum (gray scale) and high-velocity CO(3–2) emission (blue and red contours) in the center of NGC 3256. The VLA continuum image in the inset is from Neff et al. (2003, their Figure 2, reproduced by permission of the AAS) and has a resolution of $0''.63 \times 0''.15$ and contours at -0.1, 0.1, 0.15, 0.2, 0.4, 0.6, 0.9, 1.2, 2.0, and 3.5 mJy beam^{-1} (rms $\sim$27 μJy beam^{-1}). Our ALMA submillimeter data are plotted in the same way as in Figure 10(b).

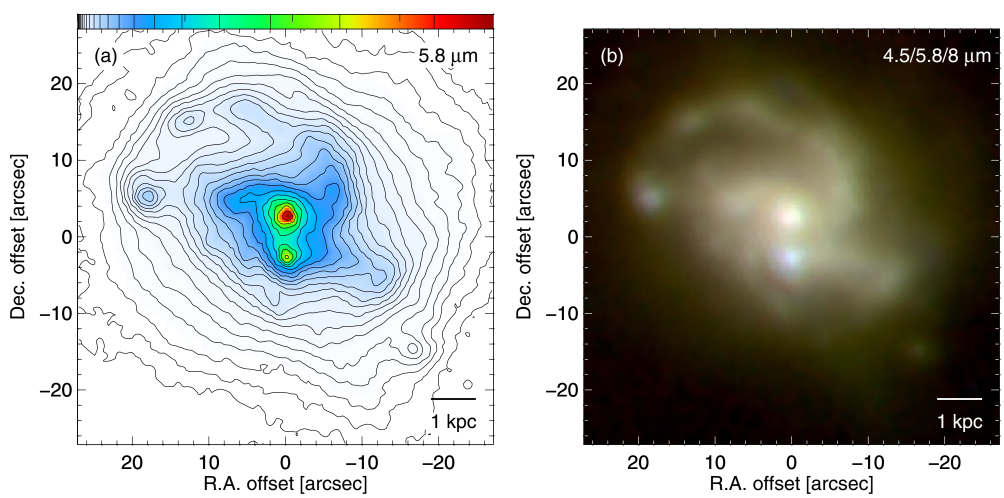

Figure 17. *Spitzer* IRAC images of the central region of NGC 3256. The area shown is the same as in Figure 1(a) for 2.8 mm continuum. (a) Continuum at 5.8 μm with contours in steps of 1/3 mag (a factor of 1.36). The intensity-to-color conversion is the same linear scaling as in the ALMA continuum images. (b) Three-color composite image made using 8, 5.8, and 4.5 μm data for red, green, and blue, respectively. The intensity-to-color conversion is logarithmic.

nuclei corresponding to the two radio and mid-infrared peaks. Their identification as the nuclei of merging galaxies is strongly supported by our detection of line and continuum peaks and large velocity gradients there (Figures 1 and 7). Parameters estimated in this section are summarized in Table 8.

4.1. NGC 3256N

The northern nucleus has a nuclear gas disk with a low inclination and nearly circular rotation, showing a clear butterfly pattern in the velocity field (Figure 7). In Section 3.2.2, we measured the disk major axis of p.a.(N) $\approx 75^\circ$ and inclination $i_{\rm N} \approx 30^\circ$. The nucleus is surrounded by molecular spiral arms, which are shown in gray in Figure 18. Therefore, there should be a gas disk containing the nucleus and the arms. Trancho et al. (2007) deduced this from kinematics of young star clusters. This northern disk must be close to face-on and coplanar with the nuclear disk judging from the arm morphology. Its near side must be the southeastern side assuming trailing arms.

4.2. NGC 3256S

The southern nucleus must be nearly edge-on and in front of the northern galaxy disk. The large inclination is inferred from the extinction peak toward this nucleus, suggesting internal extinction, the lack of a clear butterfly pattern in the velocity field (Figure 7), and the shape of the region that has both large optical extinction (reddening) and large CO line width in Figure 15(b). This region extends in the east–west direction across the southern nucleus, as expected when the foreground (part of the) southern galaxy has a high inclination and a major axis at p.a.(S) $\approx 90^\circ$. Such a configuration results in large line widths because of the overlap of the two galaxies and the nearly edge-on geometry of the southern disk. To the west of this red and wide-line region are the five young clusters that

Table 8
NGC 3256 Measured and Estimated Parameters

Parameter	Value	Note
Northern galaxy/nucleus:		
Inclination (°) $i_{\rm N}$	30	(1)
Major axis p.a. (°)	75 (90)	(2)
max $\Sigma_{\rm mol}$(N, 240 pc) ($M_\odot$ pc^{-2})	$4X_{20} \times 10^3$	(3)
$M_{\rm mol}$ (HV, N) ($M_\odot$)	$6X_{20} \times 10^7$	(4)
max($v_{\rm outflow,N}$) (km s^{-1})	750 (1000)	(5)
$\langle v_{\rm outflow,N} \rangle$ (km s^{-1})	300	(6)
$l_{\rm outflow,N}$ (pc)	$1\farcs8/\sin i_{\rm N} = 820$	(7)
$t_{\rm outflow,N}$ (Myr)	1.1	(8)
$\dot{M}_{\rm N}$ ($M_\odot$ yr^{-1})	$60X_{20}$	(9)
$L_{\rm kin,N}$ ($L_\odot$)	$4X_{20} \times 10^8$	(10)
$t_{\rm dip,N}$(300 pc) (Myr)	$3\chi_N$	(11)
Southern galaxy/nucleus:		
Inclination $i_{\rm S}$ (°)	80	(1)
Major axis p.a. (°)	90	(2)
max $\Sigma_{\rm mol}$(S, 240 pc) ($M_\odot$ pc^{-2})	$3X_{20} \times 10^3$	(3)
max $\Sigma_{\rm mol}$(S, 80 pc) ($M_\odot$ pc^{-2})	$6X_{20} \times 10^3$	(3)
$M_{\rm mol}$ (HV, S) ($M_\odot$)	$2.5X_{20} \times 10^7$	(4)
$\theta_{\rm S,op}$ (°)	20	(12)
max($v_{\rm outflow,S}$) (km s^{-1})	$2600c_{80}$	(5)
$\langle v_{\rm outflow,S} \rangle$ (km s^{-1})	$1400c_{80}$	(6)
$l_{\rm outflow,S}$ (pc)	$4''/\sin i_{\rm S} = 690s_{80}$	(7)
$t_{\rm outflow,S}$ (Myr)	$0.5t_{80}$	(8)
$\dot{M}_{\rm S}$ ($M_\odot$ yr^{-1})	$50X_{20}t_{80}^{-1}$	(9)
$L_{\rm kin,S}$ ($L_\odot$)	$9X_{20}c_{80}^2t_{80}^{-1} \times 10^9$	(10)
$t_{\rm dip,S}$(80 pc) (Myr)	$0.6\chi_S t_{80}$	(11)
Merger system:		
$V_{\rm sys}$ (km s^{-1})	2775	(13)
$M_{\rm dyn}$(N)/$M_{\rm dyn}$(S)	2.5 ± 1	(14)
$M_{\rm mol}$ ($r \leqslant 10''$) ($M_\odot$)	$7X_{20} \times 10^9$	(15)
$M_{\rm mol}$ ($r \leqslant 20''$) ($M_\odot$)	$1X_{20} \times 10^{10}$	(15)

Notes. We define $X_{20} \equiv X_{\rm CO}/(10^{20}\ {\rm cm}^{-2}\ ({\rm K\ km\ s}^{-1})^{-1})$, which is the ratio of the true $X_{\rm CO}$ for the gas in consideration to our fiducial conversion factor. The parameter χ is $X_{\rm CO}$(nucleus)/$X_{\rm CO}$(outflow), the ratio of $X_{\rm CO}$ between the nuclear disk and the outflow in consideration. We also define, for the southern nucleus, the ratio of trigonometric values for our most favored inclination to those for the true inclination of the southern nucleus. Namely, $s_{80} \equiv \sin 80°/\sin i_{\rm S}$, $c_{80} \equiv \cos 80°/\cos i_{\rm S}$, and $t_{80} \equiv \tan 80°/\tan i_{\rm S}$. For $i_{\rm S} = [70°, 85°]$, we have $c_{80} = [0.5, 2.0]$, $t_{80} = [2.1, 0.5]$, and $c_{80}^2 t_{80}^{-1} = [0.12, 8.0]$. (1) Inclination of the nuclear disk. (2) Major axis position angle of the nuclear disk. The number in the parenthesis for the northern galaxy is for the very center of the nuclear disk. (3) Peak molecular gas surface density of the nucleus at the given resolution. (4) The mass of high-velocity molecular gas associated with the nucleus. This only includes the gas whose line-of-sight velocity is more than 224 km s^{-1} offset from the systemic velocity. (5) The maximum outflow velocity after the correction for inclination. For the northern outflow this corresponds to the $>3\sigma$ CO(1–0) emission in Figure 8 and the number in parenthesis is from the CO(1–0) FWZI in Figure 12. For the southern outflow this corresponds to the $>4\sigma$ CO(3–2) emission in Figure 10(a). (6) Characteristic outflow velocity that we used to calculate kinematical luminosity. (7) Extent of the outflow on each side of the nucleus. This is corrected for the outflow inclination. (8) Outflow timescale, i.e., travel time. (9) Molecular mass outflow rate. (10) Kinetic luminosity of the molecular outflow. (11) Timescale for the outflow to deplete molecular gas from the nuclear region of the given diameter. (12) Opening angle of the molecular outflow. (13) The systemic velocity of the merger. We also use this as the fiducial velocity for individual nuclei. (14) The ratio of the dynamical masses in the central kpc of the two nuclei. (15) Mass of molecular gas within the indicated radius on the sky from the midpoint of the two nuclei.

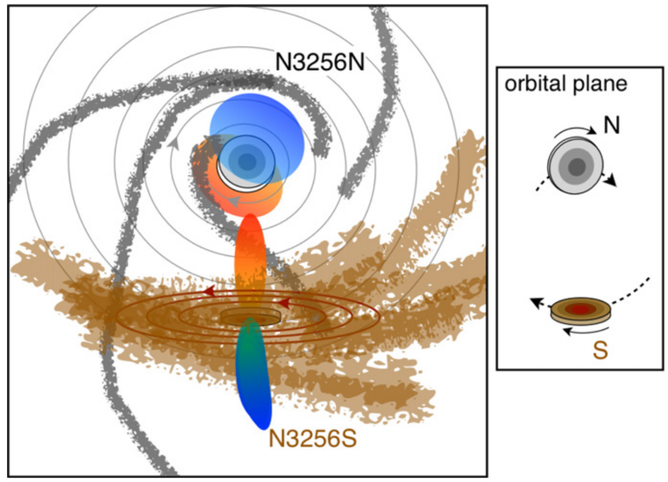

Figure 18. Illustrations of the NGC 3256 system projected to the sky plane (left) and to the orbital plane of the two nuclei (right). The sky-projected separation of the two nuclei is 0.85 kpc (5″). The northern nucleus belongs to the merger progenitor shown in gray. This component has a low inclination and has several spiral arms. The southern nucleus belongs to the merger progenitor shown in brown. This component is close to edge-on, strongly disturbed, and is slightly foreground of the northern galaxy plane. The orbital plane of the two nuclei is close to the sky plane but has its near side likely to the south. Both nuclei (and progenitors) have prograde rotation with respect to the orbital motion of the two nuclei as shown in the right panel. They have different inclinations with respect to the orbital plane and the northern nucleus is a factor of a few more massive than the southern nucleus. Both nuclei drive their own bipolar molecular outflow. They are shown as blue and red lobes for redshifted and blueshifted gas, respectively. The outflow from the northern nucleus is nearly pole-on and is wide-open. The southern outflow is nearly edge-on, well collimated, and its apparent velocity increases with distance up to about 0.3 kpc from the southern nucleus. The blue cone of the southern outflow gradually curves toward west as it leaves the nucleus.

Trancho et al. (2007) found to be out of sync with the rotation of the northern disk. It is less likely that the southern nucleus is on or behind the northern disk because we do not see a high-velocity-dispersion region with little reddening (i.e., gas behind the northern galaxy disk) in the central few kpc of the southern galaxy. The outskirts of the southern galaxy appear strongly disturbed and out of their original orbital plane judging from the large scale distribution of color excess in Figure 15(b). Near the center, a bar-like feature of molecular gas and dust crosses the southern nucleus (Figure 7, HCN in Figure 3, and Figures 1(b) and (c)). This is the edge-on southern nuclear disk in our view. For the reasons given in Section 5.2, the near side of this nuclear disk must be its northern side and the disk inclination is constrained to $70° < i_{\rm S} \lesssim 85°$.

4.3. Mass Ratio

The northern nucleus is probably a few times more massive than the southern nucleus. The ratio of the CO(3–2) line FWHM at the northern nucleus to that at the southern nucleus is 0.77 for the 4″ aperture used in Figure 12. With correction for the inclinations, this ratio reflects the mass ratio of the nuclei at 0.7 kpc scale because the broad line wings are too faint to affect the FWHM. For $i_{\rm N} \approx 30°$ and $i_{\rm S} \approx 80°$, and ignoring the effect of any difference in gas radial distributions, the mass ratio $M_{\rm N}/M_{\rm S}$ is 2.3 for the line width ratio of 0.77, and the mass ratio is between 2.1 and 2.4 for $70° < i_{\rm S} < 90°$. The line FWHM ratio increases to about 1 in larger sampling areas. The mass ratio would be 3.9 for this width ratio and $i_{\rm S}$ of 80°. This can be due to different degrees of mass concentration in the two nuclei and/or more contamination to the line width at the southern nucleus from the northern galaxy disk. With these uncertainties in mind we suggest $M_{\rm dyn}({\rm N})/M_{\rm dyn}({\rm S}) \sim 2.5$ with an error up to ± 1 for 1 kpc diameters.

4.4. Merger Orbit

Based on the widths of H I tidal tails, English et al. (2003) suggested that the merger orbital plane is almost face-on. Since the northern galaxy disk is also face-on, the southern nucleus is probably near the northern galaxy plane. This is consistent with two observations. First, the most prominent molecular arm emanating from the northern nuclear disk extends in the direction of the southern nucleus, as if bridging the two nuclei. Second, molecular arms at larger radii are around the two nuclei. The most notable one starts from the northern nuclear disk and runs east of the binary nuclei by almost 180° in our CO(3–2) map in Figure 2. These are expected to be so if the southern galaxy were close to the northern galaxy plane and exerting gravitational force on the disk gas in a direction nearly within the disk plane.

The southern galaxy has a high inclination with respect to the orbital plane in the configuration suggested above. This is consistent with much of the gas in the outer part of the southern galaxy leaving its original galactic plane because for the southern galaxy a massive perturber is on a nearly polar orbit. Direct contact of the two gas disks is another plausible reason for the disturbance, although it works on both disks. Figures 15(a) and (b) show a one-arm reddening and CO feature that starts at about 30″ east of the two nuclei and spirals into the southern nucleus after a 270° clockwise turn. This may well be material stripped from the southern galaxy tracing its past trajectory around the center of mass near the northern nucleus. If so, the southern nucleus must currently be moving from west to east (right to left in our maps).

The right panel of Figure 18 shows the two nuclear disks viewed from above the merger orbital plane. As in the sky-projection, the northern nuclear disk is close to face-on and the southern nuclear disk is nearly edge-on because the orbital plane is estimated to have a low inclination ($\lesssim 30°$) with respect to our sight line. The two galaxies have the same sense of rotation here. This prograde–prograde configuration was proposed by English et al. (2003) due to the long tidal tails (Toomre & Toomre 1972).

The gas presumably stripped from the southern galaxy and the outer gas of the northern galaxy appear to be forming a merged gas disk that is connected to the northern galaxy disk. The overall CO(1–0) velocity field in Figure 2 largely agrees with that of the northern galaxy disk regarding the kinematic major axis and low inclination, even though the outer part contains the stripped gas. Thus, the gas on the large scale appears to be settling onto the merger orbital plane that is close to the northern galaxy plane. Such a merged gas disk, proposed in SHP06, is expected to form because, unlike stars, gas is collisional and cannot remain on the original disks at the large radii where the two disks already had contact.

4.5. M_{dyn} and Gas-to-dynamical Mass Ratios

Here we calculate the dynamical masses of the two nuclear disks and an area encompassing the two nuclei. These are compared to our gas mass estimates to see whether the gas masses are reasonable.

The dynamical mass of the northern nucleus is on the order of $M_{\rm dyn}(r_{\rm N} \leqslant 200\,{\rm pc}) \sim 4 \times 10^9\,M_\odot$ on the basis of the line-of-sight rotational velocity of 150 km s^{-1} inferred from the CO PV plot (Figure 14(d)) and $i_{\rm N} \approx 30°$. The dynamical mass of the southern nucleus is estimated to be $M_{\rm dyn}(r_{\rm S} \leqslant 200\,{\rm pc}) \sim 2 \times 10^9\,M_\odot$ using the line-of-sight rotational velocity of 200 km s^{-1} inferred from the CO PV plot (Figure 14(e)) and $i_{\rm S}$ of 80°. The ratio of the two dynamical masses within 400 pc diameters is 2.2, close to the ratio of 2.5 ± 1 in 1 kpc diameters (Section 4.3). These dynamical masses have large uncertainties because we cannot accurately measure the rotational terminal velocity of each nuclear disk in the PV diagrams contaminated by the faint and broad line wings, which we attribute to outflow in the next section. We also crudely estimate the dynamical mass in the central 20″ of the merger to be $M_{\rm dyn}(r \leqslant 1.7\,{\rm kpc}) \sim 6 \times 10^{10}\,M_\odot$ from a rotational line-of-sight velocity of about 200 km s^{-1} inferred from the CO(1–0) channel maps (Figure 4) and an inclination of 30°. Although the high-velocity emission near the nuclei does not contaminate rotation on large scales, this estimate still has large uncertainty due to the assumed inclination and the possibility that some gas at this radius may not have settled.

The molecular gas masses for the same regions are estimated from CO(1–0) data to be $M_{\rm mol}$ ($r_{\rm N} \leqslant 200\,{\rm pc}) \sim 3 \times 10^8\,M_\odot$, $M_{\rm mol}$ ($r_{\rm S} \leqslant 200\,{\rm pc}) \sim 2 \times 10^8\,M_\odot$, and $M_{\rm mol}$ ($r \leqslant 1.7\,{\rm kpc}) \sim 6 \times 10^9\,M_\odot$ for $X_{20} = 1$. The gas-to-dynamical mass ratios are therefore about 6%, 12%, and 9% for the northern nuclear disk, southern nuclear disk, and the merger in its central 3.4 kpc, respectively. These ratios inherit the uncertainties of the adopted $X_{\rm CO}$ and any of its spatial variation, and any error in the dynamical masses. Since the ratios are nonetheless reasonably on the order of 10%, the 0.5 dex uncertainty for the adopted $X_{20} = 1$ seems reasonable for the bulk (though not all) of molecular gas in the observed region.

5. TWO OUTFLOWS

We argue from our observations of high-velocity molecular emission that each of the two nuclei has its own bipolar molecular outflow. In our proposed scenario, illustrated in Figure 18, activity in the northern nucleus and its low-inclination nuclear gas disk are driving a bipolar outflow with a wide opening angle in a direction perpendicular to the northern nuclear disk. This causes the high-velocity molecular line emission observed around the northern nucleus. The southern nucleus drives a more collimated bipolar outflow perpendicular to the southern nuclear disk, i.e., in the north-south direction on the sky. The high-velocity CO emission along p.a. $\sim 0°$ and 180° are due to this outflow. The receding gas in the two outflows overlaps on the sky and causes a peak of redshifted high-velocity emission between the two nuclei as seen in SHP06 and our new high-resolution observations. Outflow parameters derived in this section are also summarized in Table 8.

5.1. Northern Outflow: Uncollimated Bipolar Wind

5.1.1. Evidence, Geometry, Driving Mechanism

The following observations in Section 3.3 are evidence for a bipolar outflow with a wide opening angle from the northern nuclear disk. CO(1–0) emission is detected at $\gtrsim 4\sigma$ around this nucleus up to $|\Delta V| = 650$ km s^{-1} from the systemic and has a FWZI of about 1800 km s^{-1} (Figures 8 and 12). The high-velocity gas in CO(3–2) is detected on the northern nuclear disk with its blueshifted emission slightly shifted to the northwest and its redshifted counterpart biased toward the southeast (Figure 10(a)). These observations are consistent with the high-velocity emission being an outflow from the nucleus perpendicular to the northern nuclear disk (Figure 18).

Since the northern nuclear disk is nearly face-on, the outflow axis is close to our sightline. This pole-on viewing angle is consistent with the small spatial offset between the blueshifted and redshifted emission. This outflow must be extended, i.e., must have a wide opening angle, because it is better detected at lower resolution (in Figures 10 and 11). In particular, the blueshifted emission in Figure 11(a) directly shows that the high-velocity gas (i.e., outflow gas) is more extended around the northern nucleus than around the southern nucleus.

It is unlikely that the high-velocity gas around the northern nuclear disk is due to rotation because it has a large spatial extent and a velocity gradient along the disk minor axis. If the high velocities were rotational, the enclosed dynamical mass would be unrealistically large, although we do not exclude a small fraction of rotational high-velocity gas very close to the dynamical center. We also note that we model the high-velocity gas as outflow rather than inflow because it would be too much of a coincidence to have polar inflow simultaneously from both sides of the northern nuclear disk.

The most plausible primary driver for the northern molecular outflow is starburst in and around the northern nuclear disk. The starburst is evident and no luminous active galactic nucleus (AGN) has been found in optical, infrared, and X-ray data (Lípari et al. 2000; Lira et al. 2002, 2008; Díaz-Santos et al. 2010; Alonso-Herrero et al. 2012; Ohyama et al. 2014). Our data do not suggest the outflow originating from a particular single point such as an AGN in the nuclear disk.

5.1.2. Northern Outflow Parameters

We estimate the outflow rate from the northern nucleus to be $\dot{M}_N \approx 60 X_{20}\, M_\odot$ yr^{-1} (see Section 3.3.3 for X_{20} and that in the high-velocity gas). For this calculation, we assumed the outflow axis to have the same inclination as the northern nuclear disk, i.e., $i_{\rm N,outflow} \approx i_{\rm N} \approx 30^\circ$. The extent of the outflow along its axis is estimated to be 0.8 kpc from this inclination and the $2\farcs4$ offset between the peak of the blueshifted emission and the northern nucleus in Figure 11(b). The outflow velocity along the outflow axis is $650/\cos(30^\circ) = 750$ km s^{-1} for the largest velocity in Figure 8. The outflow timescale is therefore 1 Myr. (It is not necessarily the age of the outflow because the extent of the molecular outflow may be limited by interaction with ambient gas, dissociation of the molecules, gravity of the galaxy, and our sensitivity.) The outflow rate above is from this timescale and the mass of the high-velocity gas around the northern nucleus (Section 3.3.3). This $\dot{M}_N$ is a lower limit because it excludes the outflow at lower line-of-sight velocities than the 224 km s^{-1} cutoff in our CO flux measurement.

The kinetic luminosity of the outflow is on the order of $L_{\rm kin,N} \sim 4 \times 10^8 X_{20}\, L_\odot$ ($=2X_{20} \times 10^{35}$ W), where we use the mass of the northern high-velocity gas in Section 3.3.3, 300 km s^{-1} for a characteristic outflow velocity (i.e., 260 km s^{-1} along our sightline), and the characteristic timescale of 1 Myr. The lower velocity gas excluded from our outflow mass adds to the luminosity, but less so than to the outflow rate. The outflow kinematic luminosity is about $10X_{20}$% of the mechanical luminosity 2×10^{36} W from a half of the star formation in NGC 3256 (25 $M_\odot$ yr^{-1}, see Table 1), where we used Figure 112(b) of Leitherer et al. (1999). Therefore, the northern outflow can reasonably be driven by the starburst at and around the northern nucleus.

The gas depletion time from the northern nucleus, a 300 pc diameter region centered at the nucleus, is calculated to be $3\chi_N$ Myr from our observations. The parameter χ_N is the ratio of CO to H_2 conversion factor for the nuclear disk and that for the high-velocity gas, i.e., $X_{\rm CO}$(nucleus)/$X_{\rm CO}$(outflow), for the northern nucleus. It is 1 in our default assumption but it can be $\sim$10 if the outflow CO emission is optically thin.

5.1.3. Comparison with Previous Outflow Observations

Outflow of the interstellar medium (ISM) around the northern nucleus has been reported, and the parameters measured, in several previous works, including our detection of high-velocity molecular gas in SHP06. Scarrott et al. (1996) found with optical imaging polarimetry a dust reflection nebula extending out to 7 kpc (40″) from the galactic center and attributed it to dust entrained to the halo by a starburst-driven superwind. Moran et al. (1999) made optical slit spectroscopy across NGC 3256N and found LINER-like emission line ratios off the nucleus (up to 30″ from the center) coupled with large line widths (FWHM up to 400 km s^{-1}). They attributed these to shock-induced ionization and kinematics, and concluded the presence of a starburst-driven superwind. Heckman et al. (2000) also detected an outflow through Na D absorption lines of 550 km s^{-1} width and 309 km s^{-1} blueshift. Lípari et al. (2000) found blue wings of Hα and [N II] lines in their spectroscopy toward the northern nucleus and deduced an outflow with a velocity of $\sim$350 km s^{-1} and line width $\sim$130 km s^{-1}. Notably, the minor axis of their outflow at p.a. $\approx 70^\circ$ agrees with that of our molecular outflow, as does their wide outflow opening angle (140°). Leitherer et al. (2013) detected blueshifted line absorption of C and Si in their UV spectroscopy. Specifically, they detected three velocity components at -126, -447, and -867 km s^{-1} with the bulk velocity of -461 km s^{-1} at 2″ northeast of the northern nucleus. Our molecular outflow from the northern nucleus agrees with these observations regarding the magnitude of the outflow velocity, outflow direction and opening angle, and that the outflow has a large spatial extent. Previous reports of an outflow/superwind in NGC 3256 are probably observations of various aspects of this northern outflow, although a minor contribution from the southern outflow is likely in SHP06, and Emonts et al. (2014) recently studied the southern outflow with near-IR H_2 lines.

5.2. Southern Outflow: Molecular Bipolar Jet

5.2.1. Morphology

The southern bipolar outflow is seen as bisymmetric high-velocity emission around the southern nucleus. It lies along a p.a. $\sim 0^\circ$, and is redshifted to the north and blueshifted to the south of the nucleus (Figure 10). The outflow axis projected onto the sky is orthogonal to the nearly edge-on southern nuclear disk. We therefore assume that the outflow is along the rotation axis of the nuclear disk. Thus the near side of the southern nuclear disk must be its northern side (see Figure 18).

The southern outflow appears highly collimated. It has a compact base at the southern nuclear disk and is detected to a projected distance of $\sim$4″ (0.7 kpc) from the nucleus (Figures 10 and 5). Its length-to-width ratio is about 5 in Figure 10(b), suggesting an opening angle of about 20° for an edge-on cone (i.e., the flow is within 10° from its central axis). Since the outflow is well collimated, we call it a bipolar molecular jet.

Looking at details, the blueshifted outflow gradually curves toward the west as it goes further from the nucleus (Section 3.3.1). In our proposed scenario, this is presumably due to ram pressure, because the southern nucleus is moving from west to east with respect to the northern galaxy (Section 4.4). Similar curvature is unclear in the redshifted outflow to the north in Figure 10, but blueshifted emission to the north of the southern nucleus in the −139, −113, and −87 km s^{-1} channels in Figure 5 shows the expected curve.

The southern cone of the outflow is visible in the integrated intensity maps of CO(3–2), (2–1), and barely in CO(1–0) in Figure 2. It is also hinted at in the integrated intensity map of CN(1–0, 3/2–1/2). This feature in the integrated maps, in particular in CO(3–2), seems to have little contamination from non-outflowing ambient gas because in the channel maps it consistently maintains its spur-like morphology. This is expected for the almost edge-on southern nuclear disk; little unentrained molecular gas is expected to be at high latitudes near the galactic center. The southern cone of this outflow is also visible in the 2.1 μm line image of H_2 1–0 S(1) in Kotilainen et al. (1996, their Figure 2(a)). Emonts et al. (2014) recently found that high-velocity emission of the same line has a bipolar distribution similar to that in our CO data around the southern nucleus. They concluded this to be an outflow of hot (∼1900 ± 300 K) molecular gas.

5.2.2. Unlikely Alternatives

Before elaborating more on the southern outflow, we briefly mention two conceivable alternatives and why we do not favor them. One alternative interpretation of the gas motion around the southern nucleus is that the north–south velocity gradient is due to rotation around the nucleus. If so, the projected rotation axis of this hypothetical southern nuclear disk is along p.a. ≈ 90°. Then the continuum and line emission features along this axis, e.g., in Figures 1(b) and (c) and Figure 7(a), and the leftmost channels in Figure 10, would be polar structures, plausibly a bipolar outflow. The optical color-excess region across the southern nucleus would also be a polar structure for the southern galaxy. We reject this picture because it makes the bipolar structures much larger than the base nuclear disk. Another possible interpretation of the high-velocity gas around the southern nucleus is that it may be a merger-driven tidal feature. The tidal force exerted on the southern nucleus by the northern galaxy is along the north-south direction, i.e., the major axis direction of the high-velocity gas. We note, however, that the blueshifted high-velocity gas comes out almost directly from the southern nucleus in Figure 10(b). If the tidal force were strong enough to strip gas in the nucleus from such a small radius then the gas elongated in the east-west direction across the southern nucleus (Figure 7(a)) would not be there. Also, the merger orbital plane is close to face on (Section 4.4). Since the tidal force vector is in the orbital plane, the force cannot give large line-of-sight velocities to the tidally stripped gas. We therefore regard this alternative as equally unlikely.

5.2.3. Velocity Structure

The velocity structure of the southern outflow is noteworthy in that the highest velocity emission at $|V - V_{\rm sys}| \sim 400$ km s^{-1} is offset from the nucleus in both the blueshifted and redshifted velocities by about 1″.8 (310 pc on the sky), as we noted in Section 3.3.1. Approximately the same offsets are seen at $|V - V_{\rm sys}| \sim 450$ km s^{-1} in CO(1–0). The same is also seen in the CO(3–2) PV diagram along p.a. = 0° (Figure 14(f)), in which the terminal velocity increases with distance from the nucleus until this peak. The symmetry in the blueshifted and redshifted emission suggests this is systematic rather than a coincidence. The simplest model is that the molecular outflow accelerates from the nucleus to this distance. Alternatively, it may be that only the line-of-sight velocity increases along the outflow and peaks at $d \approx$ 1″.8. We regard this as less likely but do not rule it out. The outflow line-of-sight velocity decreases further out and the true outflow velocity may also do so.

5.2.4. Inclination Correction

We estimate the most likely inclination of the southern molecular jet (and the southern nuclear disk) to be about 80° with a range of possible values between about 70° and 85°. We already deduced in Section 4.2 that the southern nuclear disk is nearly edge-on; a conservative lower limit on the inclination is 70° from the observations there. A sign for a larger inclination is that there is blueshifted emission at the location of the redshifted cone and redshifted emission at the location of the blueshifted cone (e.g., at the −113 and +69 km s^{-1} channels in Figure 5). The condition to see both blueshifted and redshifted emission in a conical outflow is $i_{\rm S,outflow} + \theta_{\rm S,op}/2 > 90°$ where $i_{\rm S,outflow}$ is the inclination of the outflow axis and $\theta_{\rm S,op}$ is the full opening angle of the cone. For the $\theta_{\rm S,op} \sim 20°$ measured above, $i_{\rm S,outflow} \gtrsim 80°$ is the inclination to barely see both blueshifted and redshifted emission in both cones. On the other hand, the data do not support $i_{\rm S,outflow} \approx 90°$ because that would make both blueshifted and redshifted emission almost equally visible in each cone. These arguments set the above-mentioned range of $i_{\rm S,outflow}$. Further refinement of the range is hampered by uncertainties in the outflow opening angle and the curvature of the outflow.

The inclination correction to the line-of-sight velocity is at least a factor of 2.9 (=1/ cos 70°), and is 5.8 and 11.4 for the $i_{\rm S,outflow}$ of 80° and 85°, respectively. With the CO detection at least up to ±450 km s^{-1} along our sightline, the maximum outflow velocity must be at least ≳1000 km s^{-1} even considering the jet opening angle of about 20°. It is plausible, though not yet certain, that the maximum velocity is as large as 2600 km s^{-1} (=450 km s^{-1}/ cos 80°). The maximum velocity is very likely larger in this southern molecular outflow than in the northern one. The large velocity also fits the description of this outflow as a molecular jet.

5.2.5. Southern Outflow Parameters

The mass outflow rate from the southern nucleus is estimated to be $\dot{M}_S \approx 50X_{20}$ and $25X_{20}\,M_\odot$ yr^{-1} for $i_{\rm S,outflow} = 80°$ and 70°, respectively, from the projected outflow extent of 4″, a characteristic line-of-sight velocity of the outflow of 250 km s^{-1}, and the gas mass estimated in Section 3.3.3. The time scale for the outflow to travel 4″ on the sky is 0.5 and 1 Myr, respectively, for $i_{\rm S,outflow} = 80°$ and 70°. Adopting the same characteristic velocity, the kinetic luminosity of the southern outflow is on the order of $L_{\rm kin,S} \sim 9X_{20} \times 10^9\ L_\odot$ (=$3X_{20} \times 10^{36}$ W) and $1X_{20} \times 10^9\ L_\odot$ for $i_{\rm S,outflow} = 80°$ and 70°, respectively. This kinetic luminosity is larger than $L_{\rm kin,N}$ even though the northern nucleus is twice as luminous. It is (7–60)X_{20}% of $L_{\rm bol,\,S}(d = 3'')$ and exceeds the mechanical luminosity of the southern nucleus due to supernovae and stellar winds if $i_{\rm S,outflow} = 80°$ and $X_{20} = 1$.

The gas depletion time of the southern nucleus by this outflow is only $0.6\chi_S$ Myr for the central 80 pc for $i_{\rm S,outflow} = 80°$. Here we used the peak gas surface density at the 80 pc resolution for the mass of gas to be depleted by the outflow, because the base of the bipolar molecular jet appears compact. Again the depletion time does not depend on our choice of the CO to H_2 conversion factor if the same conversion factor applies to the gas at the nucleus and in the outflow (i.e., if $\chi_S = 1$), but the timescale can be 10 times longer if the outflowing CO is optically thin ($\chi_S \sim 10$).

The outflow rate and kinetic luminosity above are lower limits in the sense that they do not account for the mass that is in the outflow but has lower line-of-sight velocities than the 224 km s^{-1} cutoff in our flux measurement of the high-velocity gas in Section 3.3.2. The gas depletion time is an upper limit for the same reason. The omission of the low-velocity gas is more significant than for the northern outflow because the de-projected cutoff velocity is larger, 1300 and 650 km s^{-1} for $i_{\rm S,outflow} = 80^\circ$ and 70°, respectively. The total gas mass in the outflow may well be an order of magnitude larger than the gas mass above our cutoff velocity. In our 0.″6 resolution integrated intensity image in Figure 2, the CO(3–2) flux in the southern cone of the southern outflow is 300 Jy km s^{-1} at distances from the southern nucleus between 1″ and 4″ along the outflow. For comparison, the CO(3–2) flux at velocities above our cutoff is only 21 Jy km s^{-1} in this outflow cone in the same data set. We used the latter value for our outflow rate calculation. Thus the omission of low-velocity flow may underestimate the outflow rate by up to an order of magnitude.

5.2.6. Possible Driver: Radio Jet

The radio images in Figure 16 suggest that the southern molecular outflow is associated with a bipolar radio jet from the southern nucleus. As noted in Section 3.4.2, the regions of high velocity CO(3–2) emission at 2775 ± 380 km s^{-1} are at the tips of a pair of linear radio features from the southern nucleus, although the southern radio spur, at least, appears to go further. The southern cone of the molecular jet is along this southern radio spur marked in Figure 16(a), and follows its westward curve. These configurations suggest that there is a bipolar radio jet from the southern nucleus and that the southern molecular jet is entrained (or accompanied) by this radio jet. If so, the apparent acceleration of molecular gas along the outflow to $d \approx 1.''8$ is plausibly due to continuous dragging of molecular gas by the high speed plasma jet.

5.3. Significance of the Outflows

Both molecular outflows are significant in the mass consumption budget of the individual nuclei. It is because the outflow rates are comparable to or larger than the star formation rates in the nuclei, which Lira et al. (2008) estimated to be ∼15 and $\sim 6\,M_\odot$ yr^{-1} for the northern and southern nuclei, respectively, by modeling their infrared SEDs.[11] The total outflow rate, $60X_{20,\,\rm N\,outflow} + 50X_{20,\,\rm S\,outflow}\ M_\odot$ yr^{-1}, is also on the same order as the total star formation rate of NGC 3256, $\sim 50\,M_\odot$ yr^{-1} (Table 1). This is still so when X_{20} is ∼0.1 in both outflows for optically thin CO emission. The star formation history of the merger should be influenced by the molecular gas outflow—this was a conclusion of SHP06 and it still holds in this study.

Part of the outflowing molecular gas, in particular that in the southern molecular jet, will probably escape from the original galaxy but may not leave the merger. The ratio of escape velocity to circular orbital velocity is 2.5–3 for extended mass distributions of galaxies (Leitherer et al. 2013), whereas it is $\sqrt{2}$ for Keplerian motion. In Section 4.5 we estimated the rotational velocities of 300 km s^{-1} and 200 km s^{-1} at a radius of 200 pc for the northern and southern galaxies, respectively. Assuming a flat rotation curve in each galaxy beyond this radius, the ratio is 2.5 and 13, respectively, for the maximum molecular outflow velocity that we estimated for $\gtrsim 4\sigma$ emission in Sections 5.1.2 and 5.2.5 (i.e., 750 km s^{-1} for N and 2600 km s^{-1} for S). The ratio is 3.3 for the ∼1000 km s^{-1} maximum velocity obtained from the FWZI of the CO(1–0) spectrum on the northern nucleus. It is 7.5 (3.2) for our 1300 (650) km s^{-1} de-projected cutoff velocity used for the southern jet with $i_{\rm S,\,outflow} = 80^\circ$ (70°). A tiny fraction of the molecular gas in the northern outflow and most of the high-velocity molecular gas in the southern outflow are therefore above their respective escape velocities from the galaxies. Whether the molecular gas will escape from the merging system is a different issue and not certain. For one thing, the escape velocity from the merger is larger than that from a constituent galaxy because the former is more massive. Moreover, hydrodynamical effects on the outflowing molecular gas, already implied by the curvature of the southern molecular jet, are likely significant and can decelerate the outflow through interaction with ambient gas in the system.

6. DORMANT? AGN IN THE SOUTHERN NUCLEUS

The most plausible driver of the southern bipolar molecular jet is entrainment by bipolar radio jet associated with an AGN in the southern nucleus. AGNs are known to drive well-collimated radio jets of several 100 pc to several 100 kpc. The contrast between the northern and southern outflows in terms of the outflow opening angle, velocity, and kinetic luminosity also implies different driving mechanisms between them.

6.1. Constraints on Current AGN Activities

6.1.1. From the Literature

Searches have yielded no luminous AGN in the optically hidden southern nucleus, and reports have been mixed for low-luminosity AGN. Infrared spectroscopy and photometry mainly using *Spitzer* data did not find a luminous AGN in either nucleus; Alonso-Herrero et al. (2012) set a 1% limit on the contribution of any AGN to the bolometric luminosity of NGC 3256. In X-rays, Lira et al. (2002) detected both nuclei with Chandra but found no evidence for an AGN in either nucleus. Their absorption-corrected 0.5–10 keV luminosity of the southern nucleus was at least two orders of magnitude below that of classical Seyfert nuclei, i.e., at or below the luminosities of LINERs. Pereira-Santaella et al. (2011) used *XMM-Newton* observations to conclude the absence of a luminous Compton-thick AGN, noting that the weak 6.4 keV Fe Kα line marginally detected by Jenkins et al. (2004) was confirmed but too weak compared to continuum for a luminous AGN. On the positive side, Neff et al. (2003) found that the radio-to-X-ray ratios of both nuclei are indicative of low-luminosity AGNs, although they also noted the ratio at the northern nucleus may be due to an extreme nuclear starburst. Most recently, Ohyama et al. (2014) revisited the mid-IR analysis using *Spitzer* data and high-resolution (0.″36) mid-IR spectroscopy of Díaz-Santos et al. (2010). Through SED fitting to starburst and AGN templates they suggested an AGN in the southern nucleus with $L_{8\text{–}1000\,\mu\rm m} \sim 10^{9.7}\,L_\odot$, which is

[11] The star formation rates (SFRs) in the same ∼3″ apertures at the northern and southern nuclei are ∼4 and $\sim 2\,M_\odot$ yr^{-1}, respectively, for the bolometric luminosities of Ohyama et al. (2014) and the SFR calibration of Murphy et al. (2011). The difference must be in data calibration, SED modeling, and SFR calculation.

at about the upper limit of Alonso-Herrero et al. (2012). Their key diagnostics are infrared colors, in particular the 4.5 μm excess as well as the very deep 9.7 μm silicate absorption, whose absorption index is $S_{9.7\,\mu\mathrm{m}} = \ln(f_{9.7\,\mu\mathrm{m,obs}}/f_{9.7\,\mu\mathrm{m,cont}}) < -3.0$ (Martín-Hernández et al. 2006; Díaz-Santos et al. 2010, see their Figure 3 for the mid-IR data for the index). This index value is comparable to those of Arp 220 and NGC 4418 both of which have been suspected to hide Compton-thick AGNs (Roche et al. 1986; Spoon et al. 2007).

6.1.2. From ALMA Observations

The mean absorbing column density is as high as $\log(N_{\mathrm{H,equiv.}}/\mathrm{cm}^{-2}) \approx 23.5$ toward the central 80 pc of the southern nucleus, which is half of the total column density. Although this does not make the nucleus Compton thick, it is an order of magnitude larger than the column density that Lira et al. (2002) used for absorption correction. The true column density toward the AGN, if it is such, can depart much from this mean value because an AGN may be shrouded at a much smaller scale.

Any Compton thick and warm absorber around an AGN in the southern nucleus must be very compact. The compactness is implied by the fact that we did not detect a bright dusty core with a size of tens of parsecs, high opacity at submillimeter wavelengths, and $\gtrsim$100 K brightness temperature at 860 μm nor do we detect lines from vibrationally excited molecules (Table 4), unlike toward Arp 220 and NGC 4418 (Sakamoto et al. 2008, 2010, 2013; Costagliola & Aalto 2010; Martín et al. 2011). For example, a dust shroud having 860 μm opacity of 0.3 (i.e., X-ray Compton opacity $\sim$10) and a temperature 100 K should have the size of 6 pc (0$''$.03) so that it has an observed peak 860 μm brightness temperature of 0.24 K at our 0$''$.43 resolution. The bolometric luminosity of this core would be $2 \times 10^9\ L_\odot$. While this is an order-of-magnitude calculation, it is an upper limit because only a part of the 860 μm continuum is thermal dust emission (Section 3.1) and probably only a part of the observed 860 μm dust continuum is from the central 6 pc. The absence of a bright submillimeter core in our data is therefore consistent with the low luminosity of any buried AGN in NGC 3256. A less obscured AGN is not well constrained with (sub)millimeter emission, but should be visible at shorter wavelengths.

Our observations hint at some radio excess in the southern nucleus. The 860 μm spectral index suggests a sizable contribution from emission other than dust thermal emission. It may be due to synchrotron emission from the central 170 pc (Section 3.1). In addition, the two nuclei have about the same 3 mm flux density at $\sim$3$''$ resolution despite the northern nucleus being twice as luminous in L_{bol}. The 3 mm luminosity-to-L_{bol} ratio of the northern nucleus agrees with that of M82 and NGC 253, $\log(\nu L_\nu/L_{\mathrm{bol}}) \approx -5.1$ at 100 GHz. The ratio for the southern nucleus is twice as large, again hinting at a slight radio excess.

6.2. AGN Activities in the Recent Past?

The molecular bipolar jet plausibly driven by an AGN combined with the absence of luminous AGN could be explained in two ways. One is that the low-luminosity AGN is very efficient in driving the radio and molecular jets and the other is that the AGN was previously active but is currently inactive, possibly due to the quenching effect of the outflow.

There are, indeed, observations that arguably suggest a luminous AGN in NGC 3256 some 10^4 years ago. Moran et al. (1999) found, in addition to signs of a several 100 km s^{-1} superwind, broad Hα line emission with FWZI $\approx$ 4000–6000 km s^{-1} at off-center positions. The broad line is absent on the northern nucleus, but is visible $\gtrsim$10$''$ from it on both sides in a 2$''$.5 slit along p.a. = 155°. There is little velocity shift of the broad line between the two sides of the nucleus. Although the unusually large line widths and the lack of velocity shift alone could be attributed to our southern outflow, the broad line was detected outside the 20° opening angle of the outflow. Moran et al. (1999) determined it implausible that the broad line emission is reflected light of an AGN broad line region, citing the lack of a luminous AGN that can illuminate the scattering ISM several kpc away. However, it is possible, given our detection of a high-velocity molecular jet, that the southern nucleus had a luminous AGN until very recently.[12] If the broad line emission at least 3 kpc away from the southern nucleus is a light echo of the past activity, the nucleus was (much more) active 10^4 years ago. Similar variations of AGN luminosity at 10^3–10^5 year timescales have been found in a growing number of galaxies (Keel et al. 2012). In our Galaxy, the X-ray luminosity of Sgr A* dropped from its "high" state of the last 500 years by 4–6 orders of magnitude within the last 100 years (Ryu et al. 2013).

A caveat of the scenario that the southern outflow was driven by a radio jet from a recently dimmed AGN is that AGN radio jets are not preferentially aligned with the galaxy rotation axes (Kinney et al. 2000; Gallimore et al. 2006), though a good alignment was recently reported for Sgr A* (Li et al. 2013). The southern outflow and the southern nuclear disk appear aligned in the sky projection. Unless this is another case of intrinsic galaxy–jet alignment, it probably suggests collimation by the nuclear disk. It may be through interaction of a radio jet and the nuclear gas concentration, perhaps through which the jet is loaded with molecular gas. Alternatively, the alignment might be because the outflow is not entrained by a radio jet but driven by some other mechanisms, including a compact starburst, AGN, or a combination where the nuclear disk works as a collimator. Star formation in the southern nucleus is intense. Its mean luminosity surface density is $10^{4.7}\ L_\odot\ \mathrm{pc}^{-2}$ in a 500 pc aperture (Ohyama et al. 2014) and is very likely an order of magnitude or more larger in the compact $\sim$100 pc scale core, where the gas mean surface-density is as high as $\Sigma_{\mathrm{mol}}(\mathrm{S}) = 6 \times 10^3 X_{20}\, M_\odot\ \mathrm{pc}^{-2}$. It is therefore reasonable to expect some contribution of star formation to the southern outflow. If the southern outflow is driven mainly by starburst then the kinetic luminosity of the outflow must be much lower than the one calculated from our fiducial conversion factor and outflow inclination; these parameters must be lower than we assumed. On the whole, we regard the AGN jet-driven outflow to be a more plausible explanation than others as the main mechanism for the southern molecular jet. Some help from starburst is certain. This scenario is, however, not yet proven and needs further studies for verification and to determine the true driving mechanism(s).

7. DISCUSSION

We have reported our ALMA and SMA observations of molecular line and continuum emission in the center of NGC 3256. We constrained the configuration of the two merger

[12] It is also logically possible that a luminous AGN was in the northern nucleus. Integral field spectroscopy is needed to determine the spatial distribution of the broad line and its origin.

nuclei and their nuclear molecular disks much better than before and, for the first time, resolved the high-velocity molecular gas in the merger into two molecular outflows from the two nuclei.

We have suggested that the southern molecular outflow from NGC 3256S is driven by an AGN bipolar jet. If confirmed, it joins a small group of outflows that share the same driving mechanism and have been imaged in molecular line(s). They include the molecular outflows in M51 (Matsushita et al. 2004), NGC 1266 (Alatalo et al. 2011), NGC 1433 (Combes et al. 2013), and plausibly NGC 1377 (Aalto et al. 2012b) and NGC 1068 (García-Burillo et al. 2014). Compared with these outflows, the bipolar molecular jet of NGC 3256S is better collimated and more energetic for a common $X_{\rm CO}$. This may be because the AGN radio "jets" in the other galaxies are wider radio plumes. Mainly because of the large outflow velocity, the kinetic luminosity of the southern outflow approaches that of local ultraluminous infrared galaxies and quasar hosts observed by Cicone et al. (2014), who obtained outflow kinetic luminosities on the orders of 10^{36}–10^{37} W with a conversion factor three times lower than ours. The large maximum velocity of the southern outflow is also comparable to, or larger than, those in their survey, but this is probably because ours is significantly helped by the high ALMA sensitivity and the proximity of NGC 3256.

The overall significance of AGN-driven, jet-entrained molecular outflows is an open question. AGN time variability similar to what we suggest for NGC 3256S may reduce the apparent AGN contribution to galactic molecular outflows. Regarding jet-entrained outflows, on one hand, radio jets have been found only in a minority of AGNs. For instance, Ho & Ulvestad (2001) found "linear" structures of radio continuum in $14/52 = 27\%$ of optically selected, nearby Seyfert galaxies. On the other hand, the parameters of our southern outflow imply that a jet-entrained outflow can be more powerful and efficient than other outflows when normalized by the source bolometric luminosity. It is possible, therefore, that the small number and/or short lifetime of the outflows driven by AGN radio jets are offset to some extent by their efficiencies and luminosities. The two molecular outflows in NGC 3256 are excellent targets for such assessment because we can simultaneously study properties and driving mechanisms of two powerful molecular outflows of different natures.

Our observations have added two similarities between NGC 3256 and Arp 220 in addition to both being late-stage mergers with large infrared luminosities. One is the presence of outflows from both merger nuclei; for Arp 220, blueshifted molecular line absorption indicative of outflow has been detected toward both nuclei (Sakamoto et al. 2009). The other is that the two merger nuclei with less than 1 kpc projected separation still retain their nuclear gas disks with misaligned rotational axes; this was first imaged for Arp 220 by Sakamoto et al. (1999). Our submillimeter observations also revealed a clear difference between the two mergers. Namely, the nuclei of NGC 3256 are less obscured than the Arp 220 nuclei in terms of gas and dust column density averaged at a 100 pc scale. This is most clearly seen in the submillimeter continuum emission, which has an opacity due to dust of almost unity at 860 μm toward the nuclei of Arp 220, but about two orders of magnitude lower toward the nuclei of NGC 3256. In order for NGC 3256 to evolve into Arp 220, therefore, significant gas accretion is needed to the nuclei despite the ongoing strong molecular outflows that would deplete the gas in the nuclei in a few Myr. Such evolution may indeed occur because, judging from their nuclear separations, Arp 220 is probably more advanced as a merger than NGC 3256. NGC 3256 may become more luminous in that process, perhaps as luminous as Arp 220, because there is a statistical trend for larger nuclear obscuration (i.e., more gas funneling to the nuclei) and larger total luminosities in more advanced mergers (Haan et al. 2011; Stierwalt et al. 2013). Further studies on NGC 3256 are also warranted for the purpose of tracing the late evolutionary path of a merger that is plausibly about to become ultraluminous.

Finally we reemphasize our caution on $X_{\rm CO}$ in particular for the high-velocity molecular outflows. The large line widths of the outflow gas reduce the CO column density per line width, and hence may well result in optically thin CO emission. The conversion factor for that case is $X_{20} \sim 0.1$. Such a low conversion factor for optically thin CO has been adopted, for example, for the molecular outflow in NGC 1266 on the basis of multi-line CO excitation analysis (Alatalo et al. 2011). The outflows in NGC 3256 may have a similar situation and $X_{\rm CO}$. Alternatively, the outflowing gas may consist of an ensemble of optically thick (in CO) clouds that cover a wide velocity range. Partially supporting this is our detection of CN(1–0) lines, with likely enhancement relative to CO(1–0), in the high-velocity gas (Section 3.3.4). Although CN may be subthermally excited, the detection of a line with a 10^6 cm^{-3} critical density implies gas clumping for dense gas to exist in the high-velocity outflows. Even if individual clumps are not virialized as assumed for the standard $X_{\rm CO}$, the conversion factor for optically thick clumps will be larger than that for optically thin CO (while lower than the $X_{\rm CO}$ for virialized CO-thick clouds). Similar clumping and presence of dense gas in a galactic molecular outflow have been deduced for Mrk 231 by Aalto et al. (2012a) from their detection of broad line wings in HCN, HCO$^+$, and HNC lines. Since most outflow parameters in Table 8 depend on X_{20}, we need follow-up studies on the physical and chemical properties of the high-velocity gas.

8. SUMMARY

Our primary findings are:

1. Each of the two merger nuclei has its own nuclear disk where molecular line and continuum emission peak. The northern nuclear disk is nearly face-on ($i \sim 30°$), has a $\sim$200 pc characteristic radius, and clearly rotates around the northern nucleus. The southern nucleus has a more compact emission peak and a linear structure extending $\sim$200 pc on either side. It is deduced to be a nearly edge-on nuclear disk rotating around the southern nucleus. The mean molecular gas surface densities of both nuclei are about $3X_{20} \times 10^4\ M_\odot\,{\rm pc}^{-2}$ at 240 pc resolution, where X_{20} is the CO-to-H_2 conversion factor in the unit of $10^{20}\ {\rm cm}^{-2}\ ({\rm K\,km\,s}^{-1})^{-1}$. The peak gas surface density is $6X_{20} \times 10^4\ M_\odot\,{\rm pc}^{-2}$ at the southern nucleus at 80 pc resolution.
2. The high-velocity molecular gas previously found at the center of the merger is resolved into two molecular outflows associated with the two nuclei. We detected not only CO but also CN lines with enhancement in these outflows. The CN detection in a galactic outflow is the first, to our knowledge. The total molecular outflow rate of the two outflows is on the same order of the total star formation rate in NGC 3256.
3. The molecular outflow from the northern nuclear disk is a bipolar flow with a wide opening angle and a nearly pole-on viewing angle. It has de-projected outflow velocities

up to $750\,\mathrm{km\,s^{-1}}$ at $\gtrsim 4\sigma$ and an outflow time scale (crossing time) of 1 Myr. It has a molecular gas mass of $6X_{20} \times 10^{7}\,M_{\odot}$, a mass outflow rate $60X_{20}\,M_{\odot}\,\mathrm{yr^{-1}}$, and a kinetic luminosity on the order of $4X_{20} \times 10^{8}\,L_{\odot}$. The last three are for the gas at de-projected velocities above $260\,\mathrm{km\,s^{-1}}$. At the current rate, the outflow would deplete molecular gas in the northern nuclear disk in 3 Myr if the same conversion factor applies to the nuclear disk and the outflow. Most of the outflow/superwind signatures found so far at other wavelengths in NGC 3256 must be from this outflow.

4. The molecular outflow from NGC 3256S is a well collimated bipolar jet with a $\sim 20°$ opening angle and is nearly edge on. It has a de-projected maximum velocity $2600\,\mathrm{km\,s^{-1}}$ for a favored inclination angle 80° or $1300\,\mathrm{km\,s^{-1}}$ for $i = 70°$. The line-of-sight outflow velocity increases with distance up to 300 pc from the nucleus. This molecular jet has a 0.5 Myr crossing time, a mass of $2.5X_{20} \times 10^{7}\,M_{\odot}$, a mass outflow rate $50X_{20}\,M_{\odot}\,\mathrm{yr^{-1}}$, and a kinetic luminosity on the order of $90X_{20} \times 10^{8}\,L_{\odot}$ for $i = 80°$. These are for gas at projected velocities above $220\,\mathrm{km\,s^{-1}}$ and the lower velocity gas in the outflow may be an order of magnitude larger in mass. The gas depletion time for the central 80 pc is $\sim$0.6 Myr under the same assumption about the conversion factor as above and ignoring the lower velocity flow.
5. The northern outflow is a starburst-driven superwind in all likelihood. The southern outflow is most likely entrained by a radio jet from a weak or recently dimmed AGN in the southern nucleus. Evidence for the southern outflow driver includes the large differences in the outflow parameters from the northern superwind, off-nuclear broad Hα lines in NGC 3256, and a pair of radio spurs from the southern nucleus that matches the shape of the southern molecular bipolar jet.
6. Continuum spectral indices are negative at 3 mm and positive at 0.86 mm for both nuclei. The index is lower, in particular at 0.86 mm, for the southern nucleus, suggesting significant synchrotron and/or free–free emission even at 860 μm. Neither nucleus has a bright ($T_{\mathrm{b}} > 10$ K) dust continuum core of several 10 pc size at 860 μm such as those found in Arp 220 and NGC 4418. This disfavors the presence of a highly Compton-thick and currently luminous AGN in the nuclei of NGC 3256.

We are grateful to the people who worked to make ALMA a reality. We also thank the ALMA and SMA staff who carried out our observing runs, made the data assessments, and helped us at the help-desk. Detailed comments by the referee helped to clarify this paper. This paper made use of the following ALMA data: ADS/JAO.ALMA#2011.0.00002.SV and ADS/JAO.ALMA#2011.0.00525.S. ALMA is a partnership of ESO (representing its member states), NSF (USA), and NINS (Japan), together with NRC (Canada), NSC, and ASIAA (Taiwan), in cooperation with the Republic of Chile. The Joint ALMA Observatory is operated by ESO, AUI/NRAO, and NAOJ. This paper also uses observations made with the Submillimeter Array, which is a joint project between the Smithsonian Astrophysical Observatory and the Academia Sinica Institute of Astronomy and Astrophysics, and is funded by the Smithsonian Institution and the Academia Sinica. This research is also partly based on observations made with the NASA/ESA *Hubble Space Telescope*, and obtained from the Hubble Legacy Archive, which is a collaboration between the Space Telescope Science Institute (STScI/NASA), the Space Telescope European Coordinating Facility (ST-ECF/ESA), and the Canadian Astronomy Data Centre (CADC/NRC/CSA). This research has made use of the NASA/IPAC Infrared Science Archive, which is operated by the Jet Propulsion Laboratory and California Institute of Technology, under contract with the National Aeronautics and Space Administration. The authors also made use of the NASA/IPAC Extragalactic Database (NED), NASA's Astrophysics Data System (ADS), and the splatalogue database for astronomical spectroscopy. K.S. was supported by the Taiwanese NSC grants 99-2112-M-001-011-MY3 and 102-2119-M-001-011-MY3.

Facilities: ALMA, SMA, HST, Spitzer, VLA

APPENDIX

CHANNEL MAPS OF WEAK LINES

Figures 19 and 20 show channel maps of CN and CH_3CCH lines in our ALMA bandpass.

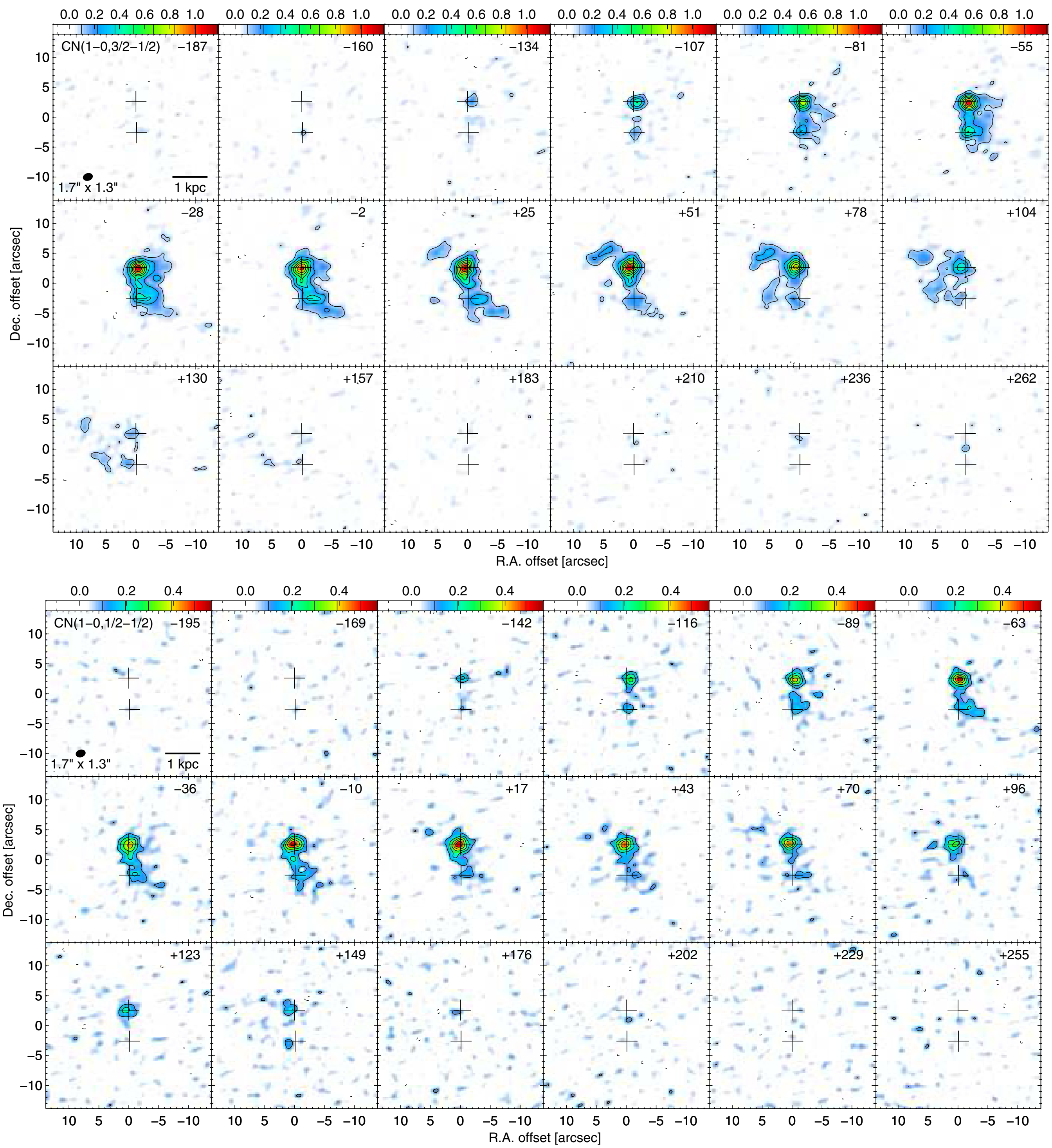

Figure 19. CN($N = 1$–0) channel maps. (top) $J = 3/2$–$1/2$ line at $f_{\rm rest} = 113.4949$ GHz. (bottom) $J = 1/2$–$1/2$ line at $f_{\rm rest} = 113.1688$ GHz. Offsets from 2775 km s^{-1} are at the top-right corners. Contours are at $\pm 3n^p\sigma$ ($n = 1, 2, 3, \cdots$), where the power p and the rms noise σ are $p = 1.2, \sigma = 32$ mK for $J = 3/2$–$1/2$ and $p = 1, \sigma = 33$ mK for $J = 1/2$–$1/2$. Negative contours are dashed. The data are not corrected for the primary beam response, whose FWHM is 54 arcsec. The peak line intensity in these plots are 1.2 K and 0.56 K, respectively, for $J = 3/2$–$1/2$ and $1/2$–$1/2$. The two plus signs in each panel are at the two radio nuclei. A black ellipse in the first panel shows the FWHM size of the observing beam.

(A color version of this figure is available in the online journal.)

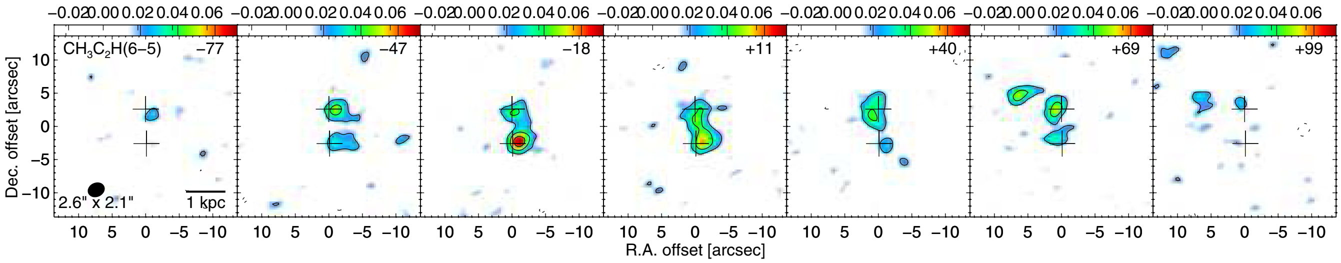

Figure 20. CH_3CCH(6–5) channel maps. Offsets from 2775 km s^{-1} are at the top-right corners. Contours are at $\pm 3n\sigma$ ($n = 1, 2, 3, \cdots$), where the rms noise is $\sigma = 7.2$ mK. Negative contours are dashed. The data are not corrected for the primary beam response, whose FWHM is 59 arcsec. The peak line intensity here is 77 mK. The two plus signs in each panel are at the two nuclei. A black ellipse in the first panel shows the FWHM size of the synthesized beam.

(A color version of this figure is available in the online journal.)

REFERENCES

Aalto, S., Booth, R. S., Black, J. H., & Johansson, L. E. B. 1995, A&A, 300, 369
Aalto, S., Garcia-Burillo, S., Muller, S., et al. 2012a, A&A, 537, A44
Aalto, S., Muller, S., Sakamoto, K., et al. 2012b, A&A, 546, A68
Aalto, S., Polatidis, A. G., Hüttemeister, S., & Curran, S. J. 2002, A&A, 381, 783
Alatalo, K., Blitz, L., Young, L. M., et al. 2011, ApJ, 735, 88
Alonso-Herrero, A., Pereira-Santaella, M., Rieke, G. H., & Rigopoulou, D. 2012, ApJ, 744, 2
Baan, W. A., Haschick, A. D., & Henkel, C. 1989, ApJ, 346, 680
Bolatto, A. D., Warren, S. R., Leroy, A. K., et al. 2013a, Natur, 499, 450
Bolatto, A. D., Wolfire, M., & Leroy, A. K. 2013b, ARA&A, 51, 207
Bryant, P. M., & Scoville, N. Z. 1996, ApJ, 457, 678
Carilli, C. L., & Walter, F. 2013, ARA&A, 51, 105
Chung, A., Yun, M. S., Naraynan, G., Heyer, M., & Erickson, N. R. 2011, ApJL, 732, L15
Cicone, C., Maiolino, R., Sturm, E., et al. 2014, A&A, 562, A21
Combes, F., García-Burillo, S., Casasola, V., et al. 2013, A&A, 558, A124
Costagliola, F., & Aalto, S. 2010, A&A, 515, A71
Díaz-Santos, T., Alonso-Herrero, A., Colina, L., et al. 2010, ApJ, 711, 328
Downes, D., & Solomon, P. M. 1998, ApJ, 507, 615
Emonts, B., Piqueras-Lopez, J., Colina, L., et al. 2014, A&A, in press (arXiv:1409.4468)
English, J., Norris, R. P., Freeman, K. C., & Booth, R. S. 2003, AJ, 125, 1134
Feruglio, C., Maiolino, R., Piconcelli, E., et al. 2010, A&A, 518, L155
Fischer, J., Sturm, E., González-Alfonso, E., et al. 2010, A&A, 518, L41
Gallimore, J. F., Axon, D. J., O'Dea, C. P., Baum, S. A., & Pedlar, A. 2006, AJ, 132, 546
García-Burillo, S., Combes, F., Usero, A., et al. 2014, A&A, 567, A125
García-Burillo, S., Martín-Pintado, J., Fuente, A., & Neri, R. 2000, A&A, 355, 499
Haan, S., Surace, J. A., Armus, L., et al. 2011, AJ, 141, 100
Heckman, T. M., Lehnert, M. D., Strickland, D. K., & Armus, L. 2000, ApJS, 129, 493
Ho, L. C., & Ulvestad, J. S. 2001, ApJS, 133, 77
Jenkins, L. P., Roberts, T. P., Ward, M. J., & Zezas, A. 2004, MNRAS, 352, 1335
Keel, W. C., Chojnowski, S. D., Bennert, V. N., et al. 2012, MNRAS, 420, 878
Kinney, A. L., Schmitt, H. R., Clarke, C. J., et al. 2000, ApJ, 537, 152
Kotilainen, J. K., Moorwood, A. F. M., Ward, M. J., & Forbes, D. A. 1996, A&A, 305, 107
Laine, S., van der Marel, R. P., Rossa, J., et al. 2003, AJ, 126, 2717
Leitherer, C., Chandar, R., Tremonti, C. A., Wofford, A., & Schaerer, D. 2013, ApJ, 772, 120
Leitherer, C., Schaerer, D., Goldader, J. D., et al. 1999, ApJS, 123, 3
Li, Z., Morris, M. R., & Baganoff, F. K. 2013, ApJ, 779, 154
Lípari, S., Díaz, R., Taniguchi, Y., et al. 2000, AJ, 120, 645
Lira, P., Gonzalez-Corvalan, V., Ward, M., & Hoyer, S. 2008, MNRAS, 384, 316
Lira, P., Ward, M., Zezas, A., Alonso-Herrero, A., & Ueno, S. 2002, MNRAS, 330, 259
Martín-Hernández, N. L., Schaerer, D., Peeters, E., Tielens, A. G. G. M., & Sauvage, M. 2006, A&A, 455, 853
Martín, S., Krips, M., Martín-Pintado, J., et al. 2011, A&A, 527, A36
Matsushita, S., Sakamoto, K., Kuo, C.-Y., et al. 2004, ApJL, 616, L55
McMullin, J. P., Waters, B., Schiebel, D., Young, W., & Golap, K. 2007, in ASP Conf. Ser. 376, Astronomical Data Analysis Software and Systems XVI, ed. R. A. Shaw, F. Hill, & D. J. Bell (San Francisco, CA: ASP), 127
Moran, E. C., Lehnert, M. D., & Helfand, D. J. 1999, ApJ, 526, 649
Murphy, E. J., Condon, J. J., Schinnerer, E., et al. 2011, ApJ, 737, 67
Nakai, N., Hayashi, M., Handa, T., et al. 1987, PASJ, 39, 685
Neff, S. G., Ulvestad, J. S., & Campion, S. D. 2003, ApJ, 599, 1043
Norris, R. P., & Forbes, D. A. 1995, ApJ, 446, 594
Ohyama, Y., Terashima, Y., & Sakamoto, K. 2014, ApJ, submitted
Pereira-Santaella, M., Alonso-Herrero, A., Santos-Lleo, M., et al. 2011, A&A, 535, A93
Roche, P. F., Aitken, D. K., Smith, C. H., & James, S. D. 1986, MNRAS, 218, 19
Ryu, S. G., Nobukawa, M., Nakashima, S., et al. 2013, PASJ, 65, 33
Sakamoto, K. 2013, in ASP Conf. Ser. 477, Galaxy Mergers in an Evolving Universe, ed. W.-H. Sun, C. K. Xu, N. Z. Scoville, & D. B. Sanders (San Francisco, CA: ASP), 21
Sakamoto, K., Aalto, S., Costagliola, F., et al. 2013, ApJ, 764, 42
Sakamoto, K., Aalto, S., Evans, A. S., Wiedner, M. C., & Wilner, D. J. 2010, ApJL, 725, L228
Sakamoto, K., Aalto, S., Wilner, D. J., et al. 2009, ApJL, 700, L104
Sakamoto, K., Ho, P. T. P., & Peck, A. B. 2006, ApJ, 644, 862 (SHP06)
Sakamoto, K., Scoville, N. Z., Yun, M. S., et al. 1999, ApJ, 514, 68
Sakamoto, K., Wang, J., Wiedner, M. C., et al. 2008, ApJ, 684, 957
Sanders, D. B., Mazzarella, J. M., Kim, D. C., Surace, J. A., & Soifer, B. T. 2003, AJ, 126, 1607
Sargent, A. I., Sanders, D. B., & Phillips, T. G. 1989, ApJL, 346, L9
Scarrott, S. M., Draper, P. W., & Stockdale, D. P. 1996, MNRAS, 279, 1325
Spoon, H. W. W., Marshall, J. A., Houck, J. R., et al. 2007, ApJL, 654, L49
Stierwalt, S., Armus, L., Surace, J. A., et al. 2013, ApJS, 206, 1
Toomre, A. 1977, in Evolution of Galaxies and Stellar Populations ed. B. M. Tinsley & R. B. Larson (New Haven, CT: Yale Univ. Observatory), 401
Toomre, A., & Toomre, J. 1972, ApJ, 178, 623
Trancho, G., Bastian, N., Miller, B. W., & Schweizer, F. 2007, ApJ, 664, 284
Turner, B. E. 1985, ApJ, 299, 312
Turner, B. E., & Gammon, R. H. 1975, ApJ, 198, 71
Veilleux, S., Cecil, G., & Bland-Hawthorn, J. 2005, ARA&A, 43, 769
Zenner, S., & Lenzen, R. 1993, A&AS, 101, 363
Zhang, Z. Y., Gao, Y., Henkel, C., et al. 2014, ApJL, 784, L31